The Analysis of Sea Surface Imagery for Whitecap Kinematics

JESSICA M. KLEISS AND W. KENDALL MELVILLE

Scripps Institution of Oceanography, La Jolla, California

(Manuscript received 15 October 2009, in final form 2 June 2010)

ABSTRACT

Visible sea surface images are analyzed to determine the distribution of the average length of breaking crests per unit sea surface area per unit speed increment $\Lambda(c)$. The $\Lambda(c)$ distribution offers a scale-dependent description of wave breaking that is valuable for understanding wave energy dissipation, momentum flux from the wave field to the surface currents, and air–sea fluxes of gas and sea salt aerosols. Two independent processing techniques for determining $\Lambda(c)$ from video images are implemented. In particular, the importance of the definition of the velocity of a breaking event is considered, as a single value, as a function of time, or as a function of space and time. The velocity can furthermore be defined as the full translational velocity or as the velocity normal to the breaking front. The $\Lambda(c)$ distributions resulting from various definitions of velocity, sensitivity to thresholds, observational resolution, and the effect of surface currents and long wave orbital velocity are presented. The appropriateness and limitations of the comparison of the first moment of $\Lambda(c)$ with the breaking rate are discussed. Two previous field observations of $\Lambda(c)$ give qualitatively different results: Melville and Matusov found an exponential form for $\Lambda(c)$, whereas Gemmrich et al. obtained a function that peaks at intermediate speeds and is up to an order of magnitude higher than that of Melville and Matusov. Both results can qualitatively be reproduced using the current dataset by employing the definitions of breaking velocity used in the previous studies. The authors argue that the current optimal interpretation of breaking speed resolves the breaking velocity as a function of both space and time and considers the velocity orthogonal to the breaking crest.

1. Introduction

Wave breaking plays an important role at the air–sea interface, transferring momentum from the wave field to surface currents, dissipating wave energy, injecting bubbles into the upper ocean, and producing sea spray and marine aerosols (Melville 1996). A better understanding of the occurrence and rate of wave breaking under various environmental conditions would improve our current understanding of these processes at the air–sea interface. In particular, a measure of the kinematics of the breaking waves would be useful for a more detailed description of wave energy dissipation, momentum, and gas transfer.

In 1985, Phillips proposed a statistical measure of wave breaking, $\Lambda(\mathbf{c})$, such that $\Lambda(\mathbf{c})\, d\mathbf{c}$ is the average total length per unit sea surface area of breaking fronts that have velocities in the range of $\mathbf{c}$ to $\mathbf{c} + d\mathbf{c}$. In the following discussion, $\mathbf{c} = (c, \theta)$ is the breaking velocity, with magnitude c and direction θ. It follows that the distribution of breaking lengths according to their speed of breaking is $\Lambda(c) = \int \Lambda(c, \theta) c \, d\theta$.

Phillips showed that the first moment of $\Lambda(\mathbf{c})$ can be related to the rate of breaking at a fixed location on the sea surface:

$$R = \int c\Lambda(\mathbf{c})\, d\mathbf{c}, \tag{1}$$

where R is the passage rate of breakers past a given point at the sea surface or, equivalently, the fraction of the sea surface that is ''turned over'' by wave breaking per unit time, with units of inverse seconds. Phillips also related the whitecap coverage W, the fraction of the sea surface covered with bubbles from wave breaking, to $\Lambda(\mathbf{c})$, dependent upon the time T that bubbles persist on the sea surface:

$$W = \int cT\Lambda(\mathbf{c})\, d\mathbf{c}. \tag{2}$$

Special care needs to be taken in distinguishing between active whitecap coverage W_A, which is the fraction of the

Corresponding author address: Jessica M. Kleiss, University of Washington, 3737 Brooklyn Ave. NE, Box 355672, Seattle, WA 98105-5672.
E-mail: jkleiss@u.washington.edu

DOI: 10.1175/2010JTECHO744.1

surface covered with foam patches associated with actively breaking crests, and old foam coverage W_B, which is the fraction of the surface covered with residual bubble patches and streaks (see Bondur and Sharkov 1982; Monahan 1993).

Incorporating the laboratory measurements of Duncan (1981) describing the self-similarity of quasi-steady wave breaking produced by a towed hydrofoil, Phillips also related the fifth moment of $\Lambda(\mathbf{c})$ to the average rate of energy loss per unit area by breakers with speeds between $\mathbf{c}$ and $\mathbf{c} + d\mathbf{c}$:

$$\epsilon(\mathbf{c})\, d\mathbf{c} = b\rho g^{-1} c^5 \Lambda(\mathbf{c})\, d\mathbf{c}, \tag{3}$$

where g is gravitational acceleration and b is a breaking strength parameter that Duncan estimated to be a constant approximately equal to 0.06. The c^5 scaling for the quasi-steady breaking of Duncan's experiments may be anticipated by the expression for the wave-making power of a cylinder (Lighthill 1978, p. 459), as well as geometrical and inertial arguments presented in Melville (1994), Phillips et al. (2001), Banner and Peirson (2007), and Drazen et al. (2008). These studies on unsteady breaking show that b is not a constant but may depend on the rate of focusing of the local energy density or on the steepness of the wave that is breaking. The spectral distribution of the mean momentum flux transferred from the wave field to the surface currents via wave breaking is given by

$$\boldsymbol{\tau}(\mathbf{c})\, d\mathbf{c} = \frac{\mathbf{c}}{c^2}\epsilon(\mathbf{c}). \tag{4}$$

From Eqs. (3) and (4), the momentum flux component in the direction of the wind can be written as

$$\tau(\mathbf{c}) = b\rho \cos(\theta) g^{-1} c^4 \Lambda(\mathbf{c})\, d\mathbf{c}, \tag{5}$$

where θ is the angle between the wind and the waves.

Field observations of wave breaking are difficult. The intermittent nature of breaking as well as the rough conditions that frequently accompany breaking makes in situ observations challenging. The quantity $\Lambda(\mathbf{c})$ can be calculated from remote measurements of the sea surface using video imagery that resolves the patches of foam due to breaking (Melville and Matusov 2002; Gemmrich et al. 2008; Thomson and Jessup 2009), radar measurements of backscattered sea spikes (Phillips et al. 2001), or infrared imagery of the surface temperature indicative of breaking microscale waves (Jessup and Phadnis 2005).

Field and laboratory measurements of $\Lambda(\mathbf{c})$ have displayed a rather wide range of results. Figure 1 shows a selection of published observations of $\Lambda(c)$ to date. Phillips et al. (2001) used radar backscatter, "sea spikes," to measure the speed of breaking events. They inferred the length of breaking from the distance traveled by the breaking wave (Thorpe and Hall 1983), and assumed that the direction of breaking was closely aligned with the wind direction. Because of these strong assumptions, their measurement of $\Lambda(c)$ is not a direct measurement but rather an inferred result. Their measurements were taken in winds of 9.3 m s^{-1} in a well-developed wave field.

Melville and Matusov (2002) analyzed visible video images of the sea surface from an aircraft with surface wind speeds of 7.2, 9.8, and 13.6 m s^{-1}. At a flight altitude of 450 m, the image size was approximately 400 m $\times$ 250 m, with approximately 0.6-m pixel resolution. Active whitecaps were identified using a brightness threshold, and the condition that the area of the whitecap was increasing. Each breaking event was tracked, and the velocity of the contour was determined using a method similar to particle imaging velocimetry (PIV; Raffel et al. 2007). Based on laboratory dye studies of the kinematics of breaking (Rapp and Melville 1990), the apparent motion of the bubble patches due to the aircraft motion was accounted for by assuming the rear of the turbulent patch produced by breaking was stationary to leading order. They also validated their results against a conceptual model relating the change in foam patch area to the length and time scales of breaking.

Jessup and Phadnis (2005) used infrared (IR) images of wind-driven waves in a laboratory channel to observe the thermal signature of microscale breaking waves under winds of 6.2, 8.1, and 9.6 m s^{-1}, with strongly forced conditions. They computed $\Lambda(c)$ with two different methods, settling on a PIV-based method. They addressed the issue of changing speed along the crest length of the breaking wave, and found that including the slower moving breaking near the edges of the breaking crest affected the final result of $\Lambda(c)$.

Gemmrich et al. (2008) used images from a video camera mounted on the research platform (R/P) *Floating Instrument Platform* (*FLIP*) to obtain images of whitecaps passing through the field of view. The wind speed ranged from almost calm to 15 m s^{-1}, and both developing and developed seas were encountered. The camera covered an area of only 9 m $\times$ 12 m with pixel size of 0.02 m $\times$ 0.02 m, which resolved all small-scale whitecaps but did not always capture the full breaking crest length of dominant breakers. They applied a threshold on the image intensity difference between subsequent images to identify actively breaking crests. An ellipse was fit to each actively breaking crest. The breaking length was determined by the major axis of each ellipse, and the breaking speed by the translation of the ellipse centroid. Each tracked breaking event was assigned a duration of breaking, a length of breaking equal to the maximum ellipse length, and a speed of breaking equal to

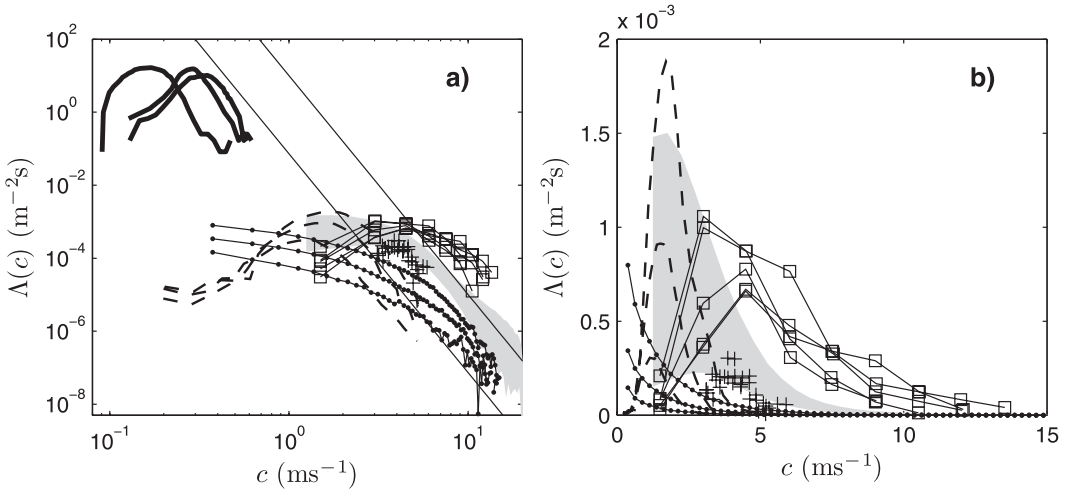

FIG. 1. Published observations of $\Lambda(c)$ to date in (a) logarithmic and (b) linear coordinates. Field observations of gravity waves are as follows: Phillips et al. (2001)—shown by crosses and inferred from radar backscatter; Melville and Matusov (2002)—shown by lines with dots, for three different wind speeds; Gemmrich et al. (2008)—shown by lines with squares, for four different sea states and winds; Thomson and Jessup (2009)—shown by dashed lines, for three different wind speeds at short fetch. Laboratory observations of microscale waves are as follows: Jessup and Phadnis (2005)—shown by thick lines, for three different wind speeds. The study presented here is shown by the gray area. In (a), the straight diagonal lines show the theoretical form of $\Lambda(c)$ from Phillips (1985) [Eq. (7) in this paper]. The lower line has $b = 0.06$, $u_* = 0.58$ m s^{-1}, and the numerical factor $4\gamma\beta^3 I(3p) = 0.0023$. The upper line is the function $10c^{-6}$.

the mean of the highest one-third of the speeds within the record, $c_{1/3}$, resulting in a distribution $\Lambda(c)$. They did not explain their choice of $c_{1/3}$ as a characteristic speed of the breaker. Gemmrich et al. found that the youngest seas showed the greatest amount of breaking near the spectral peak phase speed c_p, and all of their results show that $\Lambda(c)$ has a maximum around $0.2c_p$–$0.4c_p$.

Thomson and Jessup (2009) captured video images of the sea surface from a camera mounted 10 m above the water surface on the research vessel (R/V) *Henderson* in Lake Washington under short-fetch (7 km), young-sea ($c_p/U_{10} = 0.35$–0.45) conditions. Three case examples with winds of 6.7, 8.5, and 12.5 m s^{-1} were analyzed using a Fourier-based method to improve processing speed and reduce noise. Thomson et al. (2009) use this method to compare in situ observations of energy dissipation from acoustic Doppler velocity profiles with the wave energy dissipation estimated by $\Lambda(c)$ [Eq. (3)] for a range of field conditions in Lake Washington and Puget Sound.

For an equilibrium wave spectrum, Phillips [1985, his Eq. (6.7)] predicted that

$$\Lambda(c, \theta) = 4\gamma\beta^3 b^{-1}(\cos\theta)^{3p} u_*^3 g c^{-7}, \tag{6}$$

where γ and β are proportionality factors between the wave action source terms and p is related to the wave field directional width. Integration in the azimuthal direction yields

$$\Lambda(c) = 4\gamma\beta^3 b^{-1} I(3p) u_*^3 g c^{-6}, \tag{7}$$

where $I(3p)$ is the integral of $\cos(\theta)^{3p}$ with limits of integration from $-\pi/2$ to $\pi/2$ [Phillips 1985, his Eq. (3.5)]. This result is shown in Fig. 1. The lower solid diagonal line has $4\gamma\beta^3 I(3p) = 0.0023$, $u_* = 0.58$ m s^{-1}, and $b = 0.06$ (Duncan 1981). The upper diagonal line is simply the function $10c^{-6}$ shown throughout the paper for reference. The $\Lambda(c)$ results from the present study are shown by the gray area in Figs. 1a and 1b, under well-developed conditions ($c_p/U_{10} = 0.95$), and a wind speed of 14.9 m s^{-1}.

The importance of wave breaking for ocean surface dynamics and air–sea interaction, combined with the utility of the $\Lambda(c)$ statistic presented by Phillips (1985) have motivated recent observations of $\Lambda(c)$ in the field and laboratory, and more observations are expected in the near future. However, the wide range of results, in particular the difference between Gemmrich et al. (2008) and Melville and Matusov (2002) from video imagery, necessitate an evaluation on the methods used. In particular, we argue that the results of Gemmrich et al. (2008) and Melville and Matusov (2002) differ primarily because of the method of determining the breaking front and the definition and interpretation of the speed of breaking.

In this paper, we examine the difficulties inherent in analyzing images for the kinematics of breaking,

including the effects of brightness threshold, method of determination of the actively breaking front and the speed of breaking, the effect of averaging the speed in space and time, appropriate consistency checks, the effect of removing advection due to the underlying orbital motion of long waves and surface currents, and effects of resolution in space and time.

A single video image sequence captured from an aircraft during the Gulf of Tehuantepec Experiment (GOTEX) in 2004 is used to demonstrate the processing techniques and the resulting $\Lambda(c)$ distributions. In section 2 we describe the experimental setup used to obtain images of the sea surface from an aircraft, as well as accompanying environmental measurements. In section 3 we discuss the use of a brightness threshold to determine the extent of contours of foam produced from wave breaking. In section 4 the basic concepts of evaluating $\Lambda(c)$ from video images is presented. In section 5 the ''contour method'' to determine $\Lambda(c)$ is presented, in which the speed of breaking is resolved in both space and time around the contours (perimeters) of foam patches. The sensitivity to thresholds is addressed, as well as the effect of averaging. In particular, section 5f presents the limitations of using the relationship of the first moment of $\Lambda(c)$ to the breaking rate [Eq. (1)] as a validation tool for the $\Lambda(c)$ observations. In the later stages of this work, the paper by Gemmrich et al. (2008) was published, and so for completeness a technique similar to theirs is described in section 6 and is compared with the contour method as well as previous literature in sections 7 and 8g. In the discussion, we consider other kinematic effects at the ocean surface that may affect the observed velocity of breaking, as well as the effect of imaging resolution on the $\Lambda(c)$ results.

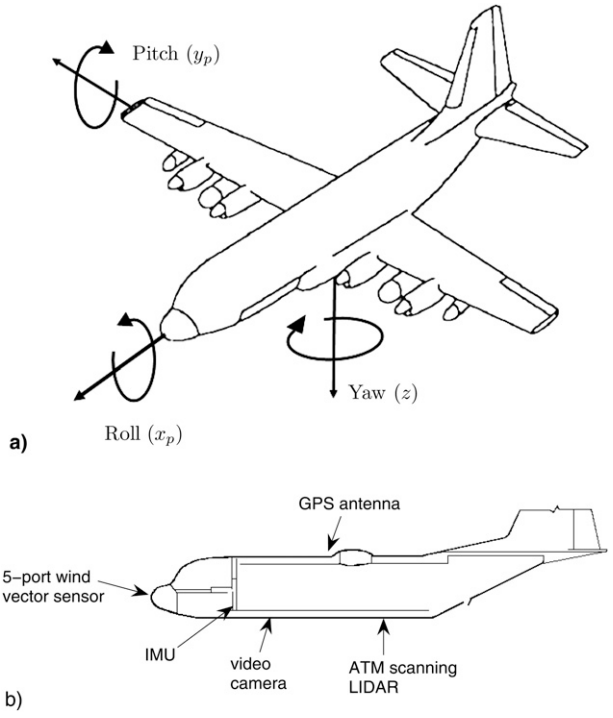

FIG. 2. (a) The aircraft coordinate system, showing the directions of the x_p, y_p, and z axes and the orientations of positive pitch, roll, and yaw angles. (b) The locations of the instrumentation on the C-130.

2. Experimental setup

A field experiment was undertaken in February 2004 in the Gulf of Tehuantepec, Mexico, which is known for strong offshore wind jets through the Chivela Pass during the wintertime (Trasviña et al. 1995; Steenburgh et al. 1998). All data were collected from the National Science Foundation–National Center for Atmospheric Research (NSF–NCAR) C-130Q Hercules aircraft. The C-130 was equipped with the standard suite of atmospheric measurements as well as an integrated optical, IR and fixed laser altimetry system, and the National Aeronautics and Space Administration (NASA) Airborne Terrain Mapper (ATM) scanning lidar (Krabill and Martin 1987; Romero and Melville 2010).

The measurements of breaking crest length and speed were obtained from images captured by a Pulnix TM-1040 digital video camera with a Computar 16–160-mm remotely adjustable zoom lens. The focal length was usually set to the 16-mm stop, and the focus set to ∞, resulting in a view angle of 31°. The camera captured 1-megapixel, 8-bit grayscale images at the maximum rate of 30 frames per second (fps), which were streamed to a personal computer (PC) through an image-foundation-class (IFC) 5.7 ''PCdig'' frame grabber. ''Video Savant'' software recorded the images to a redundant array of independent disks (RAID0) of four 250-Gbyte hard drives at a synchronized rate of either 15 or 30 fps. The time of image capture, obtained from the computer clock, was recorded for each image with a precision of 1 ms. The computer clock was synchronized hourly with global positioning system (GPS) time. The actual Δt between images had a much higher accuracy, because it was determined by the Pulnix TM-1040s internal clock, which ran at 40.068 MHz.

The orientation (pitch, roll, and yaw) of the camera was determined by the Honeywell YG1854 Laseref Special Missions (SM) inertial measurement unit (IMU) on the C-130. The IMU was located 86 cm forward and 91 cm starboard of the video camera (Fig. 2b). Any flexing of the aircraft over this small distance, as well as vibrations, would not be properly captured by the IMU and may contribute to errors in the removal of the

TABLE 1. Mean environmental conditions for the image sequence analyzed. Fetch X, aircraft altitude $A_{a/c}$, aircraft velocity $V_{a/c}$, spectral peak phase speed c_p, significant wave height H_s, 10-m wind speed U_{10}, friction velocity u_*, wind direction u_d, wave age c_p/U_{10}, number of images N, frames per second (fps), and total (nonoverlapping images) sea surface sampled A_s.

X (km)	$A_{a/c}$ (m)	$V_{a/c}$ (m s^{-1})	c_p (m s^{-1})	H_s (m)	U_{10} (m s^{-1})	u_* (m s^{-1})	u_d (°)	c_p/U_{10} —	N —	fps s^{-1}	A_s km^2
404–438	378	130	14.1	4.0	14.9	0.65	219	0.95	4059	15	7.2

aircraft motion from the image sequences.[1] The camera position was determined from the differential GPS associated with the ATM. The antenna was on the top of the aircraft, 3.75 m above and 1.6 m aft of the video camera (see Fig. 2b). The position was adjusted to the camera location using the pitch, roll, and yaw of the aircraft determined by the IMU.

The ATM scanning lidar was used to measure the surface waves and also provided aircraft positioning data when it was operating. The sea surface topography measured from the ATM yielded relevant directional spectral information about the sea state including the spectral peak phase speed c_p and the significant wave height H_s. The wave spectra had a resolution of $dk = 0.0049$ rad m^{-1}, with a noise floor cutoff of 0.35 rad m^{-1} in the dominant wave direction (Romero and Melville 2010). In this ''pilot'' experiment the map of sea surface height was not designed to be synchronized with the video imagery, but the two data streams were synchronized in postprocessing.

The wind friction velocity u_* was calculated using Reynolds stress decomposition (Brown et al. 1983) from radome gust probe measurements on the aircraft at a height of 30–50 m above sea level. The 10-m wind speed was calculated from the friction velocity and surface stability (Jones and Toba 2001; Romero and Melville 2010) assuming a constant stress layer. The winds were observed when the aircraft was flying at low altitudes, and then linearly interpolated in space to yield the wind speed and friction velocity at the location of image acquisition. The wind measurements were typically separated from the image sequence location by approximately 50 km, or 8 min.

To insure that the camera orientation obtained from the IMU and the position obtained from the GPS were properly synchronized with the time of image capture, a novel method was developed using concepts of planar homography (Ma et al. 2004; Kleiss 2009). Planar homography relates the translation of image features to the motion of the camera, assuming the object viewed is planar. Time series of the translation between sequential images, which is primarily due to aircraft motion, were compared with the expected translation computed from the camera's known position and orientation. In this way the image capture time was matched to the IMU and GPS time to within 0.004 s. This is much less than the Δt between images of 0.033 s and the Δt used for image processing of 0.133 s.

For the purpose of demonstrating the analysis techniques, a single sequence of images is considered, with environmental conditions given in Table 1. With an average altitude of 378 m, the average image size was 217 m × 215 m, and the average pixel edge size after projection was 30 cm.

3. Selection of brightness threshold

Segmenting the images into regions containing foam, active breaking, and no breaking is a difficult problem because of the wide optical dynamic range of bubbles and foam on the sea surface. Historical studies of whitecap coverage have typically used a brightness threshold to differentiate the breaking regions of the sea surface from the nonbreaking background. The regions of active breaking have a strong signal in the image *difference* of two sequential images. Two methods to compute $\Lambda(c)$ are presented in this paper: one uses a brightness threshold on the full image, and the second employs a threshold on the image difference. A full discussion of our analysis for the brightness threshold can be found in Kleiss (2009), and just the salient points are summarized here.

The normalized image intensity histogram is the probability density function $p(i)$, where i is the intensity of an image pixel. Pixel intensities have a grayscale range from black ($i = 0$) to white ($i = 1$). The fraction of the image brighter than an intensity threshold i_t is simply the complementary cumulative distribution

$$W(i_t) = 1 - \int_0^{i_t} p(i)\, di. \tag{8}$$

As i_t increases from 0 (black) to 1 (white), $W(i_t)$ decreases from 1 to 0. When viewed on logarithmic axes, the function $W(i_t)$ falls off rapidly (Fig. 3a). However, when there are foam patches present, an enhancement at higher intensities is observed, providing an indication of the appropriate choice of brightness threshold.

[1] A separate IMU rigidly mounted with the camera malfunctioned and was not available for most of the experiment.

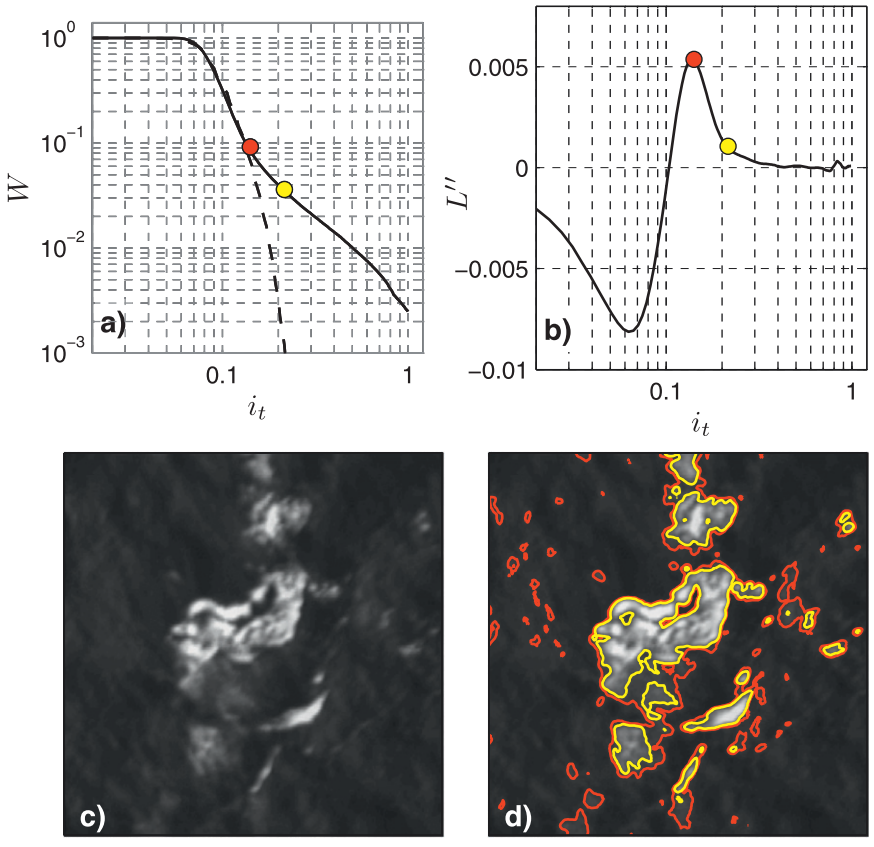

FIG. 3. Determination of the brightness threshold from the image histogram. (a) Whitecap coverage as a function of brightness threshold $W(i_t)$ for a sample image. The dashed line shows $W(i_t)$ for a different image (not shown) that contains no breaking and has been adjusted so that the mean and variance of the darkest 95% of the image matches that of the sample image. (b) The second derivative of $L(i_t)$, where $L(i_t) = \ln[W(i_t)]$. The yellow circle marks the end of the region of positive curvature, which is determined to be our brightness threshold. The red circle marks the peak curvature. (c) A portion of the sample image containing both actively breaking whitecaps and old foam patches. (d) The same image, with contours drawn at brightness intensities corresponding to the peak curvature (red), and the end of the region of positive curvature (yellow). Images (c) and (d) are 41.5 m wide × 46 m high.

Figure 3a shows the function $W(i_t)$ for a sample image (solid line), and a portion of that image is shown in Figs. 3c and 3d. The image sample contains an actively breaking whitecap (the crescent shape in the lower right quadrant), recent old foam (bright speckled patches), and older residual foam (dim patch to the left of the crescent, for example). The solid $W(i_t)$ curve does not go to zero at $i_t = 1$ because some pixels were saturated at $i = 1$, indicating a brightness beyond the dynamical range of the digital camera. In Fig. 3a the $W(i_t)$ distribution is also shown for an image containing no breaking (dashed line). Since the lighting conditions are different for the two images, the nonbreaking image has been adjusted so the mean and variance of the darkest 95% of the two images are equal for the purpose of comparison in Fig. 3a. The sensitivity of whitecap coverage on brightness intensity can be gauged from the function $W(i_t)$, shown in Fig. 3a. A brightness threshold near the yellow dot, at $i_t = 0.22$, corresponds to a whitecap coverage fraction of 0.036. Reducing the threshold by a factor of 2 results in whitecap coverage of 0.25, which is nearly an order-of-magnitude increase. Alternatively, doubling the threshold reduces the whitecap coverage to 0.13—reduction by a factor of 3.

An estimate of the curvature of $W(i_t)$ is calculated by defining $L(i_t) = \ln[W(i_t)]$ as the natural logarithm of $W(i_t)$, and taking the second derivative of $L(i_t)$ with respect to i_t, as shown in Fig. 3b. The function is smoothed with a 10-point triangular window before taking each derivative to reduce noise.

The peak in curvature, given by the red dot in Figs. 3a and 3b, initially appears to be a good choice for the brightness threshold. The resulting foam perimeters, shown in red in Fig. 3d, appear to capture the foam extent

well. However, a cluster of "false positives" is found in the upper-left corner of Fig. 3d that does not appear to consist of actual foam patches. It was found that increasing the brightness threshold i_t to the end of the region of positive curvature, as shown by the yellow dot in Figs. 3a and 3b and the yellow perimeters in Fig. 3d, avoided inclusion of the nonbreaking sea surface. From examination of images from the entire campaign, we chose the end of the region of positive curvature as the point that first falls below 20% of the peak value. Moving this cutoff closer to the peak curvature included more residual foam and streaks but also more falsely identified bright patches. A cutoff closer to the peak curvature may be appropriate for images captured under cloudy or diffuse lighting conditions. The final result is a single scalar brightness intensity threshold i_t for each image. Sequential images can be combined into a single image brightness histogram $p(i)$ to obtain a large enough sample to avoid erroneous results when individual images become filled with a large breaking event or contain no foam patches.

In practice, first the mean background lighting pattern is determined from the average of sequential images captured under steady lighting conditions, usually 4000–8000 images, representing roughly 2–4 min of image capture time or 3–6 km^2 of sea surface area. It was found that removal of the mean background lighting by pixelwise division collapsed the corrected image brightness histograms both in space and time better than pixelwise subtraction.[2] The images corrected for mean background lighting are saved and used for all further processing. The image histogram $p(i)$ is computed for each image. To account for any temporal changes in lighting, the mean of the darkest 2% of the pixels of each image is computed as $m(t)$. The histograms are shifted such that $m(t)$ is constant in time. Distribution $W(i)$ is then computed from the mean of the adjusted image histograms [Eq. (8)], and the end of the region of curvature is identified as i_t. The final brightness threshold is the mean value i_t plus the value of the temporal offset $m(t)$, resulting in a brightness threshold for each image. For the image sequence analyzed in this paper, the mean brightness intensity of all images i_t was found to be 0.45, and it varied in time from 0.42 to 0.48.

To evaluate the automatic brightness threshold, 10 volunteers manually determined the brightness threshold for 82 images sampled from diverse lighting and sea state conditions in the GOTEX experiment. The manually determined thresholds were generally centered around the automatic threshold, within a range of ± 0.12. This large range attests to the fundamental difficulty of using a single brightness threshold to differentiate breaking waves and foam patches from the unbroken sea surface. The $\Lambda(c)$ processing was repeated for values of the brightness threshold within this range, and for two values well outside this range, to fully explore the sensitivity of the $\Lambda(c)$ distribution to the choice of brightness threshold.

In the process of this work, other studies noted a similar pattern in the $W(i_t)$ function, and also used it to determine a brightness threshold. Sugihara et al. (2007) determined the brightness threshold from the region of $W(i_t)$ that was roughly constant. The GOTEX data did not indicate a region where the whitecap coverage was independent of the brightness threshold (e.g., Fig. 3a). Mironov and Dulov (2008) found that the dark end of the image intensity distribution followed a Gaussian distribution, after *subtraction* of the background image intensity. Following their methods, the GOTEX data did not show a Gaussian distribution for the darker (nonbreaking) region of the image histogram. Callaghan and White (2009) also derived an automatic threshold selection algorithm based on the image histogram.

4. Evaluation of Λ(c)

An example image containing vigorous breaking is shown in Fig. 4 on the left, with the difference of two images separated by 0.1333 s shown on the right. Region A shows a patch of residual foam left from a previously broken wave. It is not moving much, so it is barely discernible in the image difference. Region B shows a mature breaking event. The front edge of breaking is shown by the white trace in the image difference, and note that the rear of the foam patch (to the northeast) shows only minor motion. The region near C shows a cluster of actively breaking waves. The actively breaking waves show thick white regions in the image difference where they have rapidly advanced as well as dark crescents on the northeastern (rear) side of the foam caused by the forward motion of the active breaking.

Such a complicated structure as in Fig. 4 underlines the difficulty of defining the speed and length of breaking crests. Three definitions of breaking arise naturally:

1) In the elemental method, the speed $c_j(x, y, t)$ is determined at discrete points (x, y) spaced approximately at the image pixel resolution along the contour's breaking front. The elemental length of breaking $L_j(x, y, t)$ is the incremental distance between point locations (Melville and Matusov 2002).

[2] Any pixels that were fully saturated were left fully saturated, because their actual brightness was beyond the dynamic range of the image.

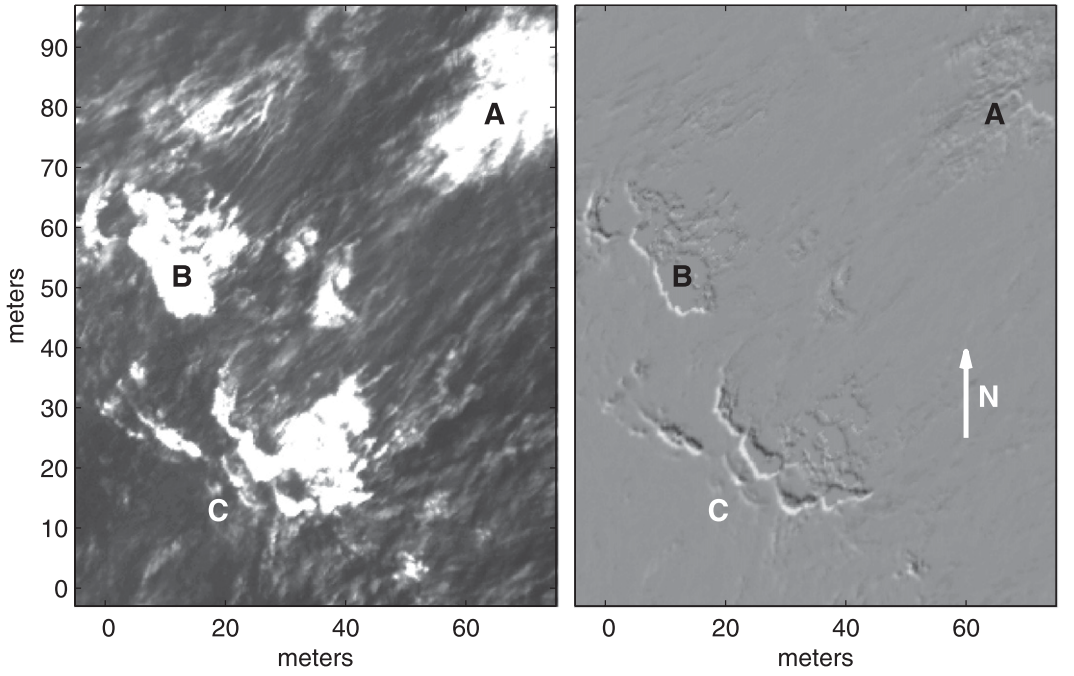

FIG. 4. (left) A sample image of the sea surface and (right) the difference of two images separated by $\Delta t = 0.1333$ s. Patch A is an old, advecting foam patch, B is a mature breaking event, and the region northeast of C contains young, active, vigorous breakers.

2) In the temporal method, $c_j(t)$ is a single measure of the speed of the actively breaking points along a breaking front at each time and $L_j(t)$ is the total breaking length each time (Jessup and Phadnis 2005; Thomson and Jessup 2009).
3) In the event method, c_j is a single estimate of speed for the entire breaking event and L_j is the sum of $L_j(t)$ (Gemmrich et al. 2008).[3]

The breaking direction could be considered on the scale of the entire foam patch, which may be dominated by translation of the foam patch (as in event C; Fig. 4), or on a local scale, which would necessitate that the breaking direction be perpendicular to the foam patch. We denote these *translational* and *normal* velocities, respectively (see Kleiss 2009, Fig. 2.6).

For all three averaging interpretations, $\Lambda(c, \theta)$ is computed as

$$\Lambda(c,\theta) = \frac{1}{A_{\mathrm{TOT}} c \Delta c \Delta\theta} \sum_j \left(L_j | c - \frac{\Delta c}{2} < c_j < c + \frac{\Delta c}{2}, \; \theta - \frac{\Delta\theta}{2} < \theta_j < \theta + \frac{\Delta\theta}{2} \right) \quad (9)$$

for all points tagged as actively breaking. Note that A_{TOT} is the total area of all overlapping images considered[4] and differs from the total (nonoverlapping) sea surface covered. The L_j and c_j are the length and speed of breaking for a given segment, observation, or event, and Δc and $\Delta\theta$ are the prescribed bin width for the $\Lambda(c)$ statistic. The omnidirectional $\Lambda(c)$ is found either by

$$\Lambda(c) = \frac{1}{A_{\mathrm{TOT}} \Delta c} \sum_j \left(L_j | c - \frac{\Delta c}{2} < c_j < c + \frac{\Delta c}{2} \right) \quad (10)$$

or, equivalently, by

$$\Lambda(c) = \int \Lambda(c, \theta) c \, d\theta. \quad (11)$$

5. Contour method

The full description of the method to project the images to an earth reference frame and extract the length and speed of breaking from airborne images of the sea surface is given in Kleiss (2009) and is summarized here for convenience.

[3] Here $\Lambda(c)\, dc$ represents the mean total length of breaking per unit sea surface area. Because the sea surface area observed A_{TOT} is the overlapping image area containing multiple observations of a breaking event, the event method length is the sum, rather than the mean, of the observed lengths $L_j(t)$.

[4] A portion of each image does not overlap the sequential image because of the translation of the aircraft and must be removed from A_{TOT} because the speed of breaking cannot be computed in this region.

To prepare the images for length and speed processing, we followed three procedures: 1) The camera lens distortion (Holland et al. 1997) was removed using the toolbox of Bouguet (2006), 2) the mean background lighting of the image sequence was removed by pixelwise division, and 3) the images were projected to an earth-centric coordinate system using the camera position and orientation at the time of each image.

To estimate the error in the earth-referenced images, each research flight day included at least one passage over the airport runway and ramp, at an aircraft altitude of approximately 500 m. The gridded lines on the tarmac served as a stationary test object. It was found that stationary objects in the earth-referenced images had a mean error (or drift) of less than 0.13 m s^{-1}, with a standard deviation of 1 m s^{-1} when the images are subsampled at 7.5 Hz, as done in this analysis (Kleiss 2009). These errors will be discussed further in section 8.

a. Identifying breaking waves in the images

Foam patches are identified on the basis of a brightness criterion, using the brightness threshold i_t as described above. A single brightness threshold applies to each image, but the threshold may change with time if the image lighting is changing. Connected pixels with brightness that exceed the threshold are grouped into objects and tracked in time under the single condition that the object edges overlap between consecutive (7.5 Hz) images. This allows foam patches to merge or break in time, without conditions on foam patch area, displacement, or continuity. Coordinates of the foam patch perimeters (contours) are saved to a file. Spurious sun glitter is short lived, so contours around patches that are tracked for less than 2/3 s are written to a different file and are excluded from further processing. At a typical flight altitude of 400 m, a point on the sea surface remains in the field of view for 1.3–2 s. While this dwell time is not long enough to observe the entire lifetime of most breaking events, $\Lambda(c)$ is a statistical description, averaged over many breaking events. It will yield a robust distribution, so long as there is no bias in the observation of events.

b. Determination of breaking speed

A method based on correlation (Raffel et al. 2007) and optical flow (Fleet 1992; Ma et al. 2004) is used to determine the velocity field at all points around the breaking contours. First, the peak of the cross-correlation function of the image gradient of two images separated by time Δt in a region centered on the contour point yields the vector difference $\Delta\mathbf{x}_{\text{corr}}$. The correlation is designed to resolve up to a 20 m s^{-1} velocity, which results in a window half-size of approximately 25 pixels, which often encompasses a large portion of the whitecap. The second image is translated by $-\Delta\mathbf{x}_{\text{corr}}$ to roughly align the breaking edge. To resolve the motion around the foam patch perimeter, a finescale translation is obtained using optical flow, which tracks points of constant brightness intensity between the two images:

$$\frac{Di(x, y, t)}{Dt} = \frac{\partial i}{\partial t} + \mathbf{u} \cdot \nabla i = 0, \tag{12}$$

where $i(x, y, t)$ is the image intensity as a function of space and time, ∇i is the spatial image gradient of the first image, $\mathbf{u} = (dx/dt, dy/dt)$ is the object motion in the image, and $\partial i/\partial t$ is the temporal derivative of the two images. Since the optical flow algorithm returns only the velocity perpendicular to the foam patch contour, if the foam patch undergoes a large translation the optical flow velocities are poorly determined. This is why the correlation first gives the bulk translation, and optical flow produces the finescale velocity fluctuations around the foam patch perimeter. The final velocity at the point is given by $\Delta\mathbf{x}_{\text{corr}}/\Delta t + \mathbf{u}$.

c. Determination of the length of active breaking

We select the actively breaking points around the perimeters of the foam patches using criteria on the image intensity, speed, and morphology at that point, as well as the evolution of the foam patch area with time $A(t)$. From all of the available breaking-wave data, we found the following criteria helped to distinguish the portion of the contour that is actively breaking from the remainder of the contour:

1) the foam patch area is increasing,
2) the image difference $i(t + \Delta t) - i(t)$ is above some threshold i_d,
3) the brightness gradient ∇i is above some threshold i_g,
4) the velocity is within $\pi/2$ of the wind direction,
5) the normal to the contour is within $\pi/2$ of the wind direction,
6) velocity is pointing outward from the contour, and
7) the contour is convex—in other words, the local radius of curvature is directed toward brighter intensity.

The first criterion considers the evolution of foam patch area. The area may show rapid changes when foam patches merge or break. On average, the time history of whitecap area for breaking events appeared to be approximately parabolic. To obtain a mean description of the area growth with time, we describe $A(t)$ for each breaking event as $\hat{A}(t) = at^2 + bt + c$ and solve for a, b, and c in a least squares sense.

All of the subsequent criteria apply to each point around the foam patch. Ultimately, any segment on a contour that passes six of the seven listed criteria was marked as actively breaking. Then the actively breaking segments are checked for continuity in space and time, such that all breaking points must be supported by neighboring breaking points in both space and time. Note that discontinuous segments around a given foam patch contour may be tagged as actively breaking.

d. *Sensitivity to thresholds of the contour method measurement of* $\Lambda(c)$

The contour method of processing utilizes four threshold criteria, in order of importance: 1) The brightness threshold i_t that identifies the extent of foam patches, 2) the threshold on the image difference i_d that aides in determining the actively breaking portion of the contour, 3) the threshold on the image gradient i_g that aides in determining the actively breaking portion of the contour, and 4) the threshold on the length of time the foam patch has been tracked t_τ that helps to distinguish foam patches from transient sun glitter. The effect of the settings for these thresholds on $\Lambda(c)$ will be discussed in this section.

To test the sensitivity of $\Lambda(c)$ to the choice of i_t, i_d, and i_g, the thresholds were varied and $\Lambda(c)$ was computed. Figure 5 shows the results for $\Lambda(c)$ when the brightness, difference, and gradient thresholds are varied. In all panels, the color corresponds to the mean brightness threshold i_t. The optimum mean threshold i_t for this image sequences is 0.45, and it is believed to be acceptable between the range of 0.33 and 0.56. Two values of the mean brightness threshold i_t well above and well below the acceptable values are also shown with dashed lines for comparison. Note that the color scale is not linear. The $\Lambda(c)$ distribution is computed using the elemental, translational velocities, corrected for the underlying long-wave orbital velocities.

Each of the three panels of Fig. 5 demonstrates $\Lambda(c)$ for a different combination of the difference and gradient thresholds i_d and i_g. The full seven criteria listed in section 5c are used to determine the portion of the foam contour that is actively breaking. In Fig. 5a, the difference threshold i_d and the gradient threshold i_g are both set to zero. This means that any segment of the contour perimeter that has an increasing brightness in the next frame passes the breaking criterion number 2. Since the magnitude of the image gradient is always positive, setting $i_g = 0$ essentially eliminates criterion number 3.

After attempting an algorithm-based definition and extensive manual inspections, an acceptable value of i_d in the range of 0.10–0.12 was found for all images. So in Fig. 5b, i_d is set to 0.12. The brightness gradient is sharper along the actively breaking portion of the foam contour than the rest of the contour, although the value changes for different breaking events. Therefore, in Fig. 5b, i_g is set uniquely for each breaking event as 1 standard deviation above the mean brightness gradient for the entire event. Using a dynamic threshold for i_g is helpful for resolving the breaking front of small, dim foam patches. However, it also increases the number of falsely identified actively breaking fronts on foam patches that are not actually breaking.

In Fig. 5c the brightness difference and brightness gradient thresholds are both set to constant values of $i_d = 0.10$ and $i_g = 0.12$, which were found from the distribution of the brightness difference and gradient around the breaking contours. Constant values of the image difference and image gradient thresholds result in $\Lambda(c)$ distributions that are less sensitive to the brightness threshold i_t. This is because the active breaking length is limited by the changing brightness (the white crescents in Fig. 4b) at the location of the foam perimeter. In particular, note that the $\Lambda(c)$ distribution with the inappropriately low brightness threshold of $i_t = 0.21$ is in better agreement with the family of $\Lambda(c)$ curves, despite the fact that it includes many bright patches of the sea surface that are not foam patches. In contrast, Fig. 5a shows the greatest sensitivity to the brightness threshold i_t. We conclude that employing breaking criteria on the changing image brightness in space (i_g) and time (i_d) using a constant threshold is a preferred processing technique.

As will be discussed below, comparison of the first moment of $\Lambda(c)$ with the breaking rate [Eq. (1)] can be a helpful internal consistency check. The acceptable range of brightness thresholds for this image sequence is 0.33–0.56, as determined by the manual validation by the 10 volunteers. This range of thresholds directly results in a breaking rate R of 0.0035–0.0171. The $\Lambda(c)$ distributions that have an intensity threshold i_t and a breaking rate R within these acceptable ranges are shown in Fig. 5d. The $\Lambda(c)$ distributions appear to be insensitive to all thresholds for the higher speeds, $5 < c < 10$ m s^{-1}, agree to within a factor of 2 and are in qualitative agreement with Phillips's expected power-law form of $\Lambda(c)$. The distributions show more uncertainty and sensitivity to the thresholds for low to medium speeds, $c <$ 5 m s^{-1}. In this experimental setup, some of this variability is due to the vibrations in the camera motion, estimated at ± 1 m s^{-1}, combined with the minimum speed resolution of 1 pixel per Δt, or 2.25 m s^{-1}. What is the cause of the reduced observations of slow breaking waves, relative to Phillips's theoretical distribution, and the resulting peak in the $\Lambda(c)$ distributions? Slower breaking waves are typically associated with shorter

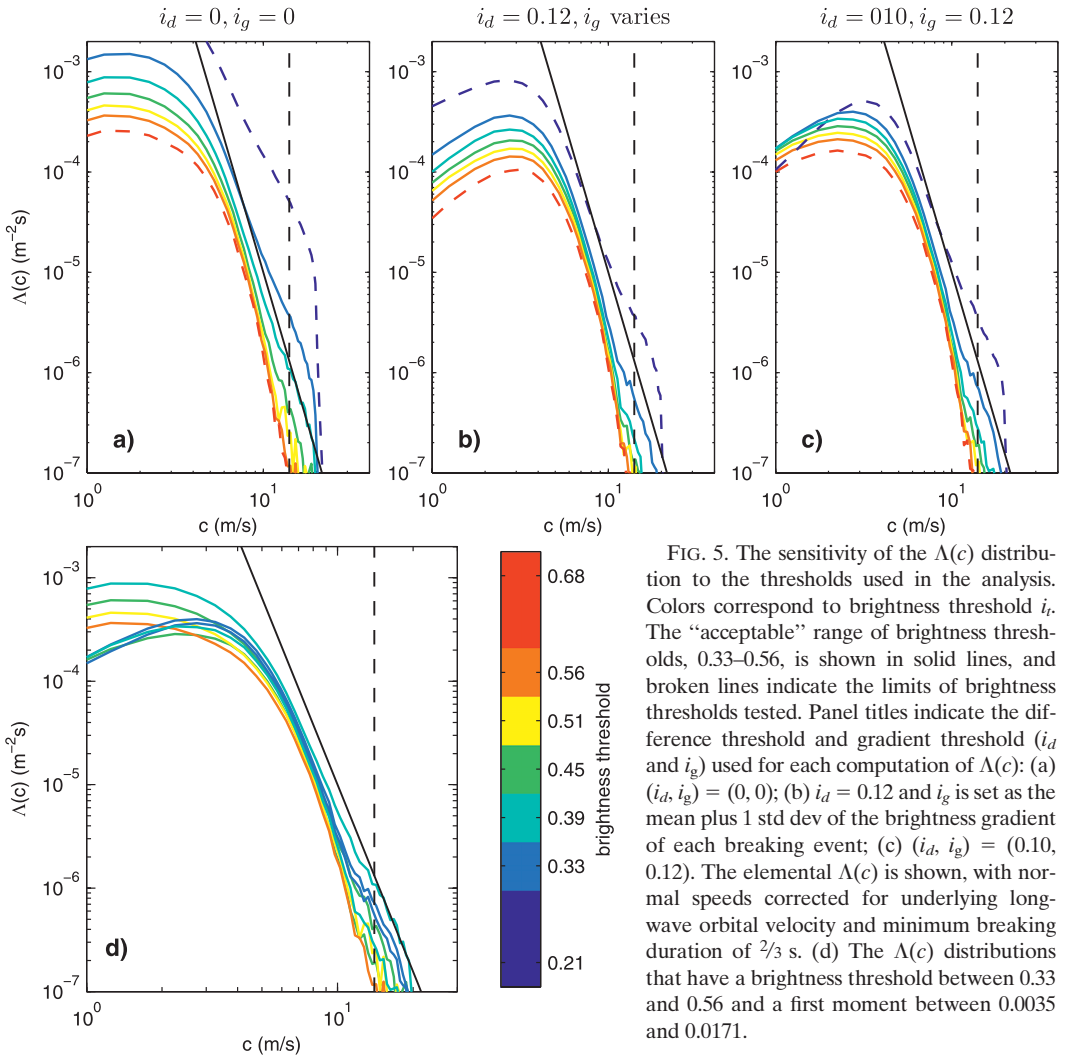

FIG. 5. The sensitivity of the $\Lambda(c)$ distribution to the thresholds used in the analysis. Colors correspond to brightness threshold i_t. The "acceptable" range of brightness thresholds, 0.33–0.56, is shown in solid lines, and broken lines indicate the limits of brightness thresholds tested. Panel titles indicate the difference threshold and gradient threshold (i_d and i_g) used for each computation of $\Lambda(c)$: (a) $(i_d, i_g) = (0, 0)$; (b) $i_d = 0.12$ and i_g is set as the mean plus 1 std dev of the brightness gradient of each breaking event; (c) $(i_d, i_g) = (0.10, 0.12)$. The elemental $\Lambda(c)$ is shown, with normal speeds corrected for underlying long-wave orbital velocity and minimum breaking duration of $^2/_3$ s. (d) The $\Lambda(c)$ distributions that have a brightness threshold between 0.33 and 0.56 and a first moment between 0.0035 and 0.0171.

wavelengths, and smaller amplitudes. They will presumably create smaller bubble patches that will appear more dim and short-lived in video images. In the extreme, small breaking waves are not expected to generate submerged bubbles at all. The observations of microscale breaking waves by Jessup and Phadnis (2005) in Fig. 1a indicate that inclusion of microscale breaking waves that have no bubble patch would result in enhanced values of $\Lambda(c)$ at small speeds.

Throughout the rest of the paper, a mean brightness threshold of 0.45, image difference threshold of 0.10, and image gradient threshold of 0.12 were used, unless otherwise noted.

e. *Effect of averaging: Interpretation of $\Lambda(c)$*

The $\Lambda(c)$ resulting from the three averaging methods is shown in Fig. 6a. The elemental method (thin line with dots) shows the broadest distribution, with segments of the breaking front surpassing the peak phase speed of 14.1 m s^{-1} (shown by the vertical dashed line). Averaging the elemental data reduces the distribution at high and low speeds and increases the distribution near the peak. Averaging also causes the high-speed tail of the $\Lambda(c)$ distribution to shrink. This is because the *event-average* method returns a single speed for a breaking event whereas the elemental method returns on the order of 100 observations of speed. A larger total sea surface area sampled would presumably lengthen the tail of the averaged $\Lambda(c)$ distributions.

In Fig. 6b, the $\Lambda(c)$ resulting from the elemental method using the full translational velocity (thin line with dots) and the normal velocity (line with open circles), which is the component of velocity perpendicular to the breaking front, is shown. The elemental method using both translational and normal speeds shows agreement for the highest speeds ($c > 6$ m s^{-1}), but the

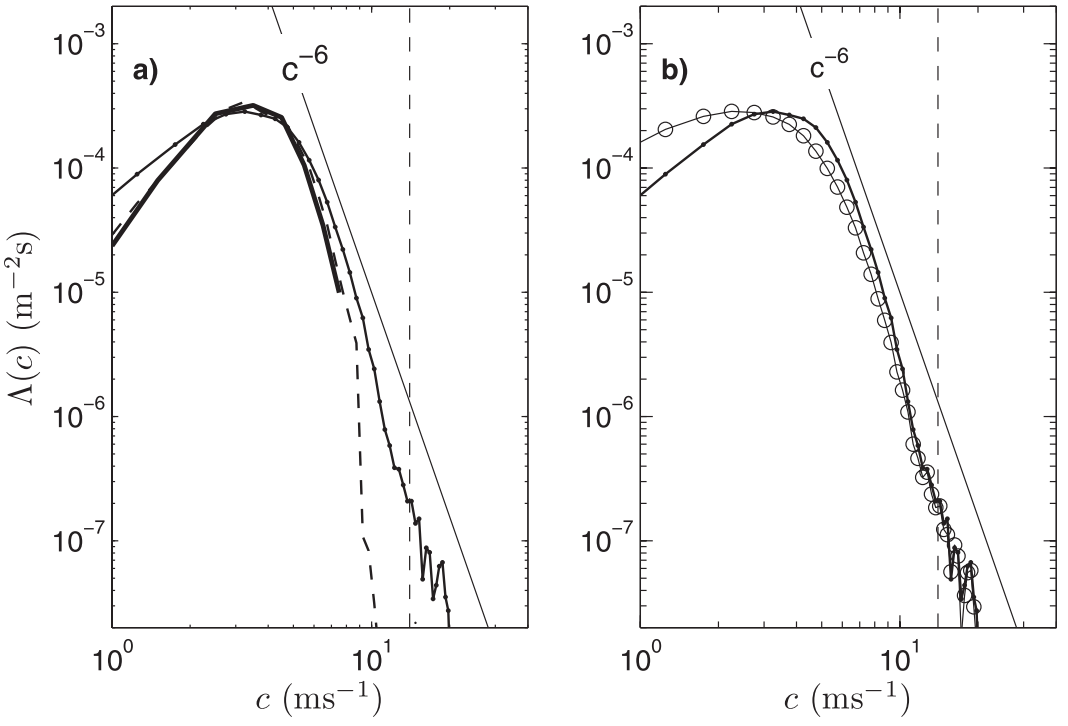

FIG. 6. The $\Lambda(c)$ distribution for the three averaging methods. The vertical dashed line indicates the peak spectral phase speed of 14.1 m s^{-1}, and the diagonal line is the function $10c^{-6}$. (a) The thin, dashed, and thick lines correspond to the elemental, temporal, and event averaged methods, respectively. Speeds are the full translational speeds from the PIV–optical flow method. (b) The thin line is the same as in (a); the line with circles shows the elemental method with the component of velocity perpendicular to the breaking front.

perpendicular component of velocity decreases the distribution for intermediate speeds and increases it for low speeds, $c < 3$ m s^{-1}. The difference primarily occurs near the edges of the breaking waves, where the normal velocity has smaller speeds and a wider angular distribution, indicative of the lateral growth of the whitecap (see also the discussion below on the directional breaking distributions). We maintain that the most accurate determination of $\Lambda(c)$ is the elemental method, with velocities orthogonal to the breaking crest. If a temporal or event-averaged estimate is desired, however, the translational speed is preferable to the normal speed.

f. First moment check

As mentioned in the introduction, the first moment of $\Lambda(c)$ should correspond to the breaking rate R [Eq. (1)]. An estimate of the total breaking rate R can be obtained from our image sequences either temporally or spatially. On the one hand, many stationary points are tracked while in our field of view. The breaking rate R is equal to the number of points ''hit'' by a breaking wave, that is, that transition from below to above the brightness threshold, divided by the total time all points reside in the images. On the other hand, R is equal to the spatial fraction of the image that transitions from nonbreaking to breaking, as determined by the brightness threshold, over some time Δt. A thorough discussion of the nuances of calculating the breaking rate is given in Kleiss (2009).

Although Eq. (1) is valid and useful, in practice both $\Lambda(c)$ and R depend sensitively upon a visible definition of wave breaking involving some choice of threshold. So this check serves as a valuable consistency check on the processing methods rather than as physical validation of $\Lambda(c)$ observations. This is demonstrated in Fig. 7. The families of $\Lambda(c)$ distributions in the three panels of Fig. 5 are represented with circles ($i_d = 0$ and $i_g = 0$) triangles ($i_d = 0.12$ and i_g is set dynamically), and squares ($i_d = 0.10$ and $i_g = 0.12$). The filled symbols correspond to the solid lines in Fig. 5, where the brightness threshold is within the acceptable range, and open symbols correspond to the dashed lines.

In Fig. 7a, the total breaking rate is determined temporally from 50 000 randomly seeded points in the image swath. The breaking rate R is directly related to the brightness threshold i_t, which is shown on the top axis. Two patterns appear in Fig. 7a. The first is the striking agreement of the first moment of $\Lambda(c)$ with the breaking

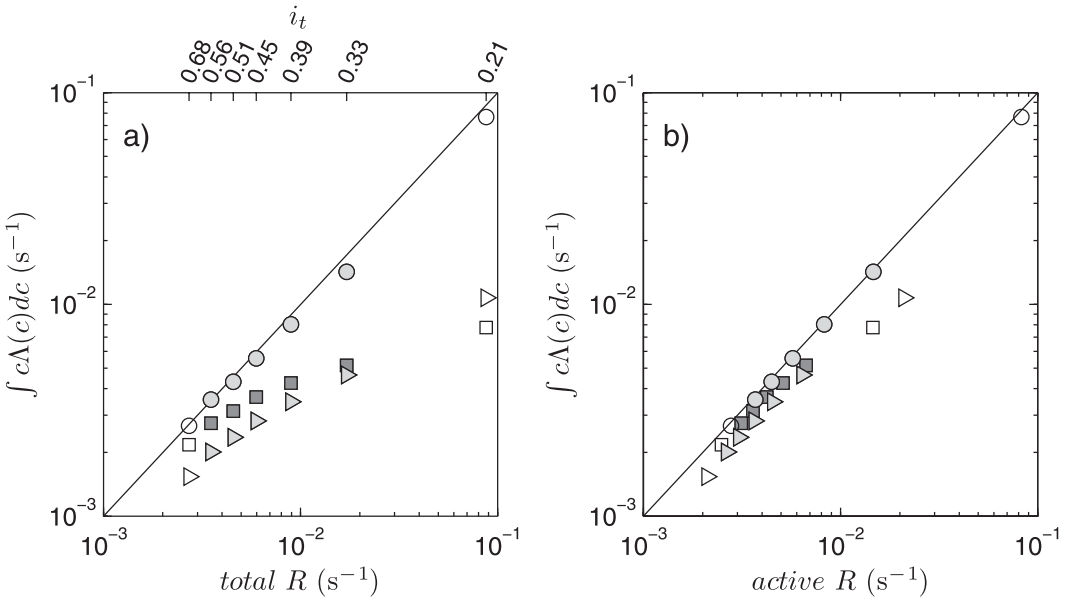

FIG. 7. Comparison of the rate of breaking R to the first moment of $\Lambda(c)$ for a range of thresholds. (a) The total breaking rate is the number of stationary points seeded in the image swath that make the transition from below to above a brightness threshold (i_t; top tick marks) per unit time. (b) The active breaking rate requires that the breaking region that contains the seeded point also contains at least one active breaking segment determined from the $\Lambda(c)$ processing. Symbols indicate the difference and gradient thresholds used in calculation of $\Lambda(c)$. Circles show i_d = 0 and i_g = 0; triangles show i_d = 0.12 and i_g set individually for each breaking event; squares show i_d = 0.10 and i_g = 0.12. The filled symbols correspond to the solid lines in Fig. 5, where the brightness threshold is within the acceptable range, and open symbols correspond to the dashed lines. The diagonal lines show a 1:1 relationship.

rate for the case in which there are fewer constraints on active breaking (circles; i_d = 0 and i_g = 0). The actively breaking portion of the foam patch perimeter is essentially determined solely by the forward motion of the foam patch. In particular, the upper open circle corresponds to the unreasonably high $\Lambda(c)$ distribution that included many nonbreaking facets of the sea surface, obtained with a brightness threshold of i_t = 0.21. Despite the obviously incorrect $\Lambda(c)$ distribution, the first moment of $\Lambda(c)$ shows excellent agreement with the breaking rate. This shows that agreement of the first moment of $\Lambda(c)$ with the breaking rate is a necessary, but not sufficient, check on the $\Lambda(c)$ processing. The second pattern apparent in Fig. 7a is that the first moment of $\Lambda(c)$ falls below the total breaking rate for the cases that have more restrictive criteria for active breaking along the foam patch perimeter (squares and triangles). These $\Lambda(c)$ distributions show less sensitivity to the brightness threshold, consistent with Figs. 5b and 5c. Manual inspection indicated that the difference was due largely to advection of large, old foam patches, such as region A in Fig. 4.

In the GOTEX image sequences the *total* breaking rate included motion of bright, old foam patches, which should not be included in the $\Lambda(c)$ distribution of active breaking. This was addressed by considering an *active* breaking rate. The active breaking rate uses the $\Lambda(c)$ analysis to differentiate active breaking from the motion of bright, old foam patches and therefore is not independent of $\Lambda(c)$. Each seeded point that makes the transition from below to above the brightness threshold is located in a spatial region of the image that made the transition above the brightness threshold; compare the white crescents in the difference image in Fig. 4. If this connected region contains at least one elemental location of active breaking, as determined from the $\Lambda(c)$ processing, the seeded point is considered to be hit by an actively breaking wave. Agreement of the active breaking rate with the first moment of $\Lambda(c)$ requires that the full length of breaking and appropriate speed of breaking have been calculated. It does not check that $\Lambda(c)$ has appropriately identified all actively breaking waves in the images, however.

In Fig. 7b, the active breaking rate is compared with the first moment of $\Lambda(c)$. The results for the case with little discrimination of active breaking (circles; i_d = 0 and i_g = 0) show little change. The results for the more-discriminating cases (squares and triangles) show improved agreement. The first moment of $\Lambda(c)$ for the preferred breaking thresholds, i_d = 0.10 and i_g = 0.12

(squares), are about 90% of the active breaking rate. The agreement degrades for the case with the unacceptably low brightness threshold of $i_t = 0.21$ (open symbols). When all GOTEX image sequences are processed with these active breaking thresholds, the active breaking rate shows good agreement with the first moment of $\Lambda(c)$, as shown in Kleiss and Melville (2010).

6. Ellipse method

A second, largely independent, method of processing was implemented based on the methods put forth in Gemmrich et al. (2008). This method identifies actively breaking wave crests on the image difference rather than the original image (see Fig. 4), and fits an ellipse to the active breaking front. Thus we call this the ellipse method. After the GOTEX images are corrected and projected to earth coordinates, the methodology of Gemmrich et al. (2008) is followed, with the following three differences. First, regions of the image difference that surpass a brightness difference threshold are grouped in space and tracked simply if they come in contact with one another. It was found that using criteria on ellipse axis orientation, magnitude of translation, and proximity as described in Gemmrich et al. (2008) failed to adequately group breaking events that merge or split in time in our dataset. Second, an ellipse is fit to the (sometimes disjoint) breaking fronts on each image that have been grouped together, rather than adding individual ellipses fit to separate breaking fronts. The ellipse is fitted by computing the central second moments of the breaking front regions on each image (Hornberg 2007).

Third, the breaking velocity is taken as the translation of the ellipse centroids *along the mean propagation direction*, rather than the total centroid translation as done in Gemmrich et al. (2008). The mean propagation direction is defined as the mean orientation of all minor axes of the ellipses in an event. The GOTEX dataset showed a large amount of noise due to lateral displacement of the breaking front and changing morphology of the breaking front over Δt. This may be due to the lower resolution of our data (~30 vs 2 cm), although the Δt for the two field experiments are similar (0.133 vs 0.1 s). It may also be due to the observed standard deviation error of 1 m s^{-1} of removal of the aircraft motion. The length of the breaking is given by the major axis of the ellipse, as in Gemmrich et al. (2008). Both the speed and length are a function of time.

The distribution of $\Lambda(c)$ from the ellipse method is shown for a range of difference thresholds i_d along with the first moment in Fig. 8. The family of $\Lambda(c)$ distributions shows the same basic shape as the difference threshold is varied. Similar to the contour method, the high-speed regime changes by only a factor of about 2 for speeds of $6 < c < 10$ m s^{-1} but varies by up to an order of magnitude for the slower speeds. The line style indicates the difference threshold i_d. As the threshold is decreased, more regions of the image difference are picked up as actively breaking wave crests.

In Fig. 8b the first moment of the $\Lambda(c)$ distributions are shown as a function of the difference threshold i_d. The first moment of $\Lambda(c)$ decreases as the threshold increases. The full rate of breaking R was calculated independently by considering the passage rate of breaking waves past many stationary points in our field of view. The breaking rate was $R = 0.006$ s^{-1} when a breaking patch was determined using our optimal choice of brightness threshold. The breaking rate resulting from the acceptable range of thresholds, $i_t = 0.33$–0.56, was $R = 0.0035$–0.0171 s^{-1}. This region is shown in gray in Fig. 8b, with the breaking rate $R = 0.006$ s^{-1} shown by the horizontal black line. The first moment of the ellipse method $\Lambda(c)$ distributions generally falls within the acceptable range of R and is on the low side. The full first moment also includes regions of the sea surface that become brighter because of advection of bright, nonbreaking foam patches. These issues are still at play in this case, so the fact that the first moment of $\Lambda(c)$ is on the low side is reasonable.

The ellipse method has relatively few thresholds to set, has a straightforward criterion to identify actively breaking waves, and is computationally faster than the contour method. Using a straight line to describe a breaking front region—which is often convoluted, curved, broken, and rapidly evolving—is a coarse approximation, however. The ellipse method also attributes a single speed to each observation of breaking, although the speed may be varying along the breaking crest. The ellipse method also contains no information about the foam patch size or shape or the speed at the rear of the foam patch.

7. Comparison of ellipse and contour methods

We compare the results from the contour method with the ellipse method. The contour method is evaluated with a mean brightness threshold of $i_t = 0.45$ and difference and gradient thresholds of $i_d = 0.10$ and $i_g = 0.12$ (as in Fig. 5c). To directly compare with the ellipse method, we consider translational speeds with temporal or event averaging. The ellipse method employs a difference threshold $i_d = 0.16$, and both methods require that the event is actively breaking for $t_\tau > 0.667$ s. The difference thresholds i_d are not the same because the contour method uses more criteria to determine active breaking, so a more lenient gradient threshold is allowable. Since the difference threshold is the only

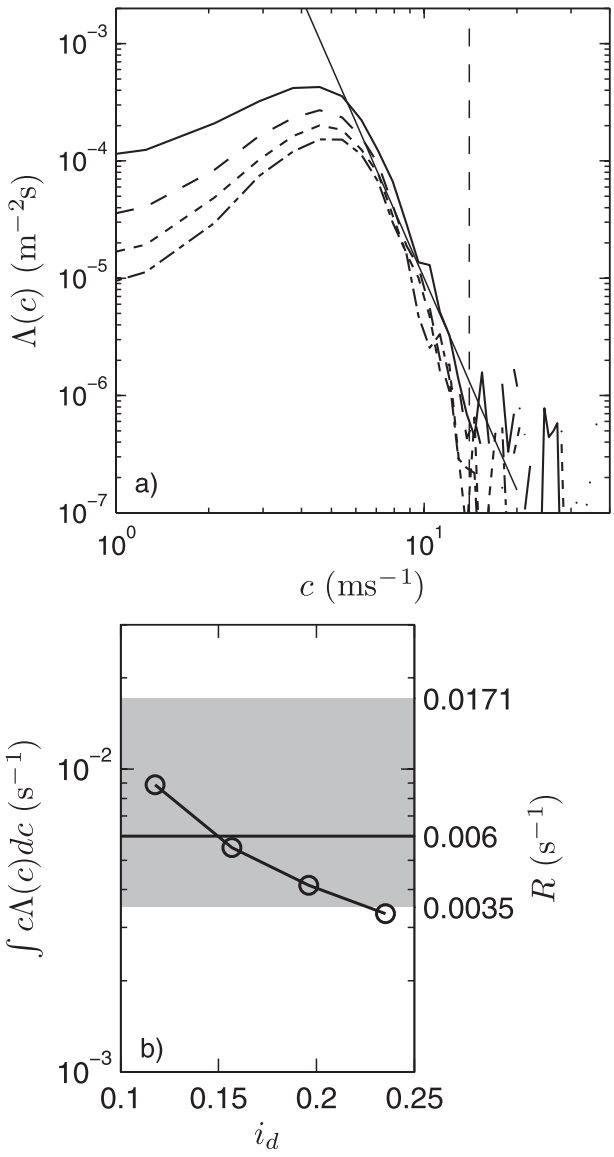

FIG. 8. (a) The $\Lambda(c)$ distributions resulting from the estimates of length and speed from the ellipse method, for a range of image difference thresholds i_d: solid line shows $i_d = 0.12$; dashed line shows $i_d = 0.16$; dotted line shows $i_d = 0.20$; dash–dotted line shows $i_d = 0.24$. The dashed vertical line at $c = 14.1$ m s^{-1} indicates the spectral peak phase speed, and the diagonal black line is the function $10c^{-6}$. (b) The first moment of the $\Lambda(c)$ distributions from (a) vs the difference threshold i_d. The gray area shows the range of acceptable breaking rates from stationary point analysis, and the horizontal black line shows the breaking rate for the optimal threshold.

threshold in the ellipse method, a less-strict threshold results in more falsely identified breaking crests.

A comparison of the contour and ellipse methods is shown in Fig. 9 for different averaging interpretations of $\Lambda(c)$. In Fig. 9a, the full resolution of both methods is shown, with no averaging: the contour method elemental speeds (translational) and the temporal ellipse method speeds. The ellipse method does not resolve elemental speeds, so this information is not available for comparison. Beneath Fig. 9a the ratio of $\Lambda_{\mathrm{ellipse}}/\Lambda_{\mathrm{contour}}$ shows the two methods agree to within a factor of 2 for speeds $0.5 < c < 10$ m s^{-1}. At higher speeds of $5 < c < 12$ m s^{-1} the ellipse method estimate is 1.3 times that of the contour method. Examination of individual breaking events indicated that this was caused by the curvature of the breaking front, which results in slower speeds along the extremities of breaking in the contour method, whereas the ellipse method assigns a single speed to the entire observation. It was also caused by small, dim, rapidly translating foam patches at the onset of breaking, which are occasionally missed by the contour method.

In Fig. 9b, the temporal $\Lambda(c)$ is shown, where each observation of breaking contributes a length and a speed of breaking to the $\Lambda(c)$ distribution. The ellipse method curve is the same as in Fig. 9a. The contour method drops precipitously at $c = 10$ m s^{-1}. The distributions have a similar form, though the ellipse method appears to be shifted toward higher speeds. However, the discrepancy is not due to a bias in the speed estimate. A detailed analysis comparing individual breaking events indicated that the speeds agreed to within 5% and that the distributions of speeds were closely matched. The determination of breaking length and duration differed substantially, however. For breaking events in which both methods found temporal speeds of greater than 6 m s^{-1}, the ellipse method on average contributed 2 times the breaking length of the contour method. For breaking events with speeds of less than 3 m s^{-1}, the contour method length of breaking was on average 50% longer than the ellipse method. So the difference between the two distributions in Fig. 9b is not due to a shift in the x direction but rather to an adjustment in the y direction. Figure 9c shows the event-average $\Lambda(c)$ for both the contour (solid) and ellipse (dashed) methods. The same qualitative picture is seen as in Figs. 9a and 9b.

In all cases, the contour method observes more slow-speed breaking for speeds in the range $1 < c < 4$ m s^{-1}, and the ellipse method observes more high-speed breaking in the range $4 < c < 10$ m s^{-1}. This is because the contour method resolves the slower edges of breaking events, while the ellipse method attributes the main translational speed of the event to the entire breaking front. Also, the contour method may include falsely identified breaking regions on the rear facets of actively breaking foam patches, which may reduce the averaged speed. Both methods may include falsely identified breaking regions associated with bright, yet nonbreaking, foam patches.

The directional distributions of $\Lambda(c)$ are shown in Fig. 10. The black arrow shows the spectral peak phase

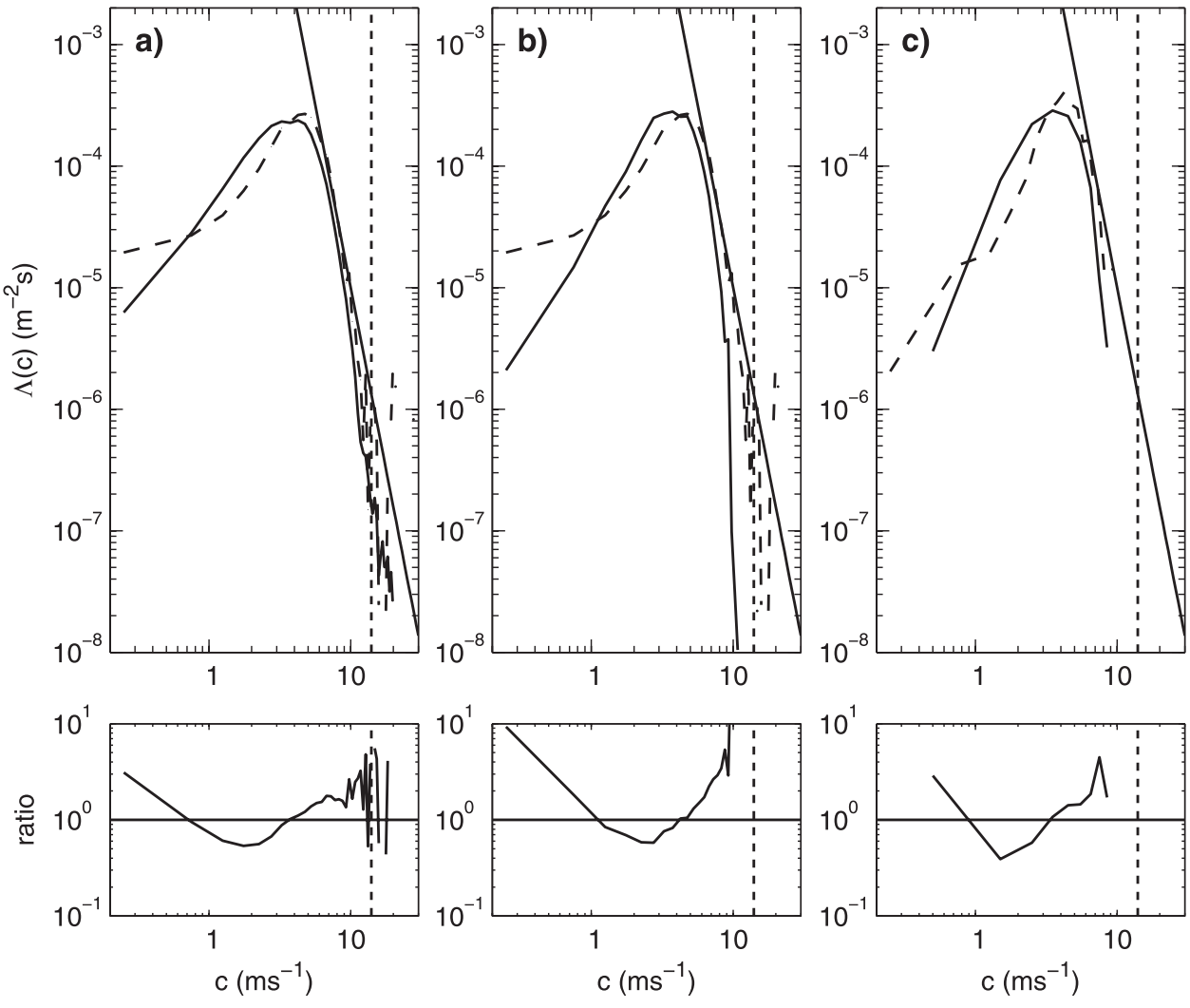

FIG. 9. A comparison of the $\Lambda(c)$ results from the contour method (solid line) and the ellipse method (dashed line) for different averaging methods: (a) no averaging: elemental speeds for contour method, temporal speeds for ellipse method; (b) temporal speeds [$c(t)$]; (c) event-averaged speeds. Beneath each comparison is the ratio of the ellipse method over the contour method for clarity. The vertical dotted line at $c = 14.1$ m s^{-1} indicates the spectral peak phase speed for this image sequence. The diagonal line in the upper panels indicates the relationship $\Lambda(c) = 10c^{-6}$, and the level line in the lower panels indicates a ratio of 1. In all cases the translational velocities are shown for the contour method.

speed and direction. The concentric dashed black circles indicate the extent of the equilibrium range. The inner circle is where the omnidirectional spectrum makes the transition from a $k^{-2.5}$ to a k^{-3} dependence (Romero and Melville 2010; Kleiss and Melville 2010), and the outer circle corresponds to 2 times the spectral peak wavenumber. Figures 10a–c show the contour method with translational velocities, and the second row shows the elemental contour method with normal velocities (Fig. 10d), as well as the ellipse method (Figs. 10e,f). The averaging style is indicated at the top of the figure. For reference, the $\Lambda(c)$ distributions shown in Figs. 9a–c correspond to Figs. 10a and 10d, Figs. 10b and 10e, and Figs. 10c and 10f, respectively. The translational velocities in Fig. 10a show a narrower distribution than the normal velocities in Fig. 10d because of the curvature of the breaking front. The ellipse method shows a qualitatively different directional distribution than the contour method. The direction of breaking is generally wider, and fewer breaking lengths are observed at slow speeds relative to the contour method. Figures 10a, 10d, and 10e show the results without averaging. The ellipse-method temporal method (Fig. 10e) shows fewer events at high speeds, but they contribute a longer crest length than the elemental methods (Figs. 10a,d). Interestingly, the azimuthally averaged $\Lambda(c)$ distributions in Fig. 9a show

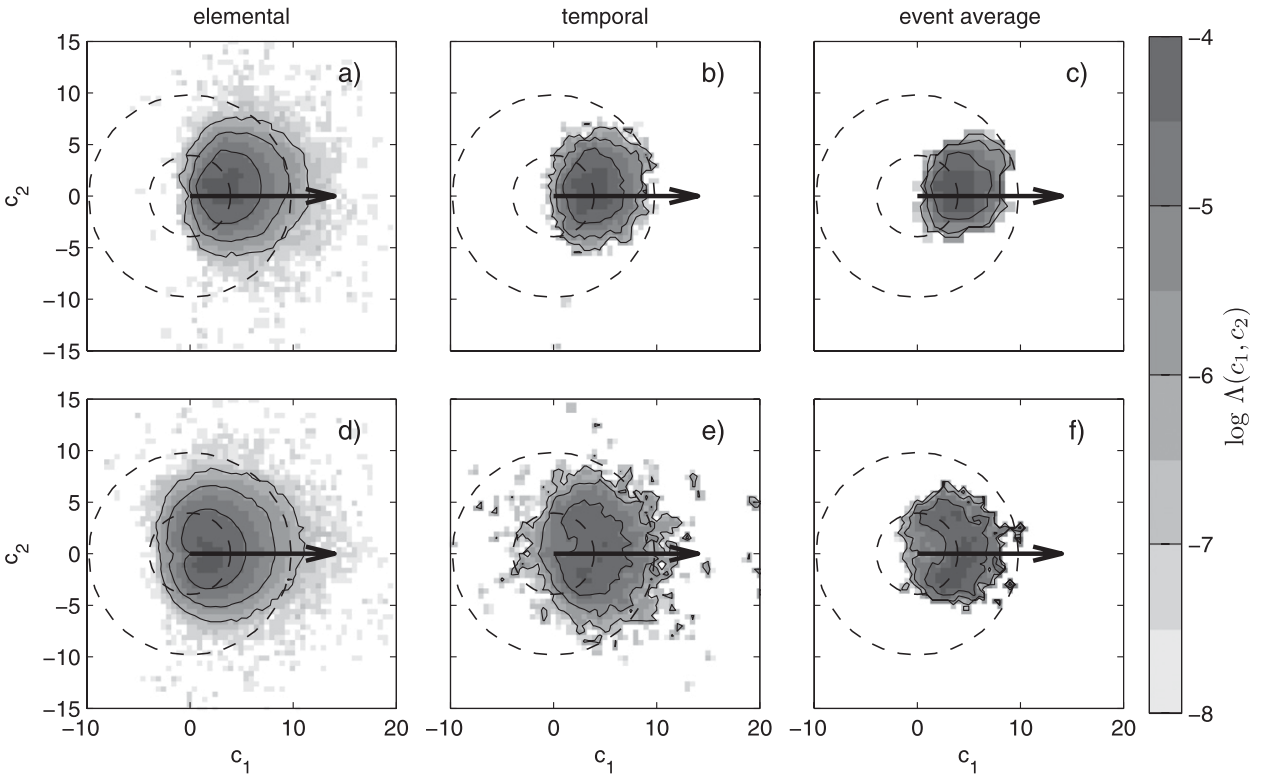

FIG. 10. The directional distributions of $\Lambda(c_1, c_2)$, where c_1 is along the dominant wave direction. (top) The contour method with translational velocities, using $i_t = 0.45$, $i_d = 0.10$, $i_g = 0.12$, and the following averaging methods: (a) the elemental method, (b) the temporal method, and (c) the event-average method. (d) The contour method with elemental, normal velocities. The ellipse method, using $i_d = 0.16$, for (e) the temporal method and (f) the event average. Black dashed concentric circles at 3.9 and 9.8 m s^{-1} indicate the estimated equilibrium region of the wave spectra. The black arrow shows the spectral peak phase speed, and contours are drawn at integer values of −5, −6, and −7.

agreement to within a factor of 2, despite the substantially different forms of the directional distributions.

8. Discussion

a. Interpretation of the speed of breaking

Central to the Phillips (1985) formulation of $\Lambda(c)$ and the energy dissipation rate from breaking waves is the assumption that the speed of breaking c is related to the intrinsic phase speed of the underlying wave and therefore to the scale of the wave that is dissipating energy. The observed breaking speed may differ from the intrinsic phase speed because of advection from long-wave orbital velocities, surface drift currents, and the inherent difference between breaking speed and underlying phase speed.

b. Correction for long-wave orbital velocity

It has been recognized that small waves are more likely to break near the crests of long waves (Longuet-Higgins 1969). When this is the case, however, the orbital velocity of the long wave affects the small wave's apparent speed of breaking. The long-wave surface orbital velocities are estimated from the sea surface elevation measurements. The scanning lidar (ATM) measures the sea surface elevation $\eta(x, y, t)$ with a horizontal spatial resolution of 5 m over a swath of sea surface that covers 96% of the image footprint. The wavenumber spectra were kindly provided by L. Romero (Romero and Melville 2010). The sea surface elevation is bandpass filtered around 0.5–3 times the spectral peak wavenumber to isolate the dominant wave signal. The Hilbert transform $H(x, y)$ is taken of the bandpass filtered wave signal, so

$$A(x, y) = [\eta^2(x, y) + H^2(x, y)]^{1/2} \quad \text{and}$$
$$\Phi(x, y) = \tan^{-1}\left[\frac{H(x, y)}{\eta(x, y)}\right], \tag{13}$$

where A is the local amplitude of the long wave envelope and Φ is the phase. Then the long-wave wavenumber vector can be computed as

$$\mathbf{K}(x, y) = \nabla\Phi(x, y),$$

and, assuming the deep-water dispersion relation, the local linear estimate of the orbital velocity at the surface is

$$\mathbf{u}_{\text{orb}} = A\mathbf{K}\sqrt{\frac{g}{K}}\cos(\Phi), \tag{14}$$

where g is the gravitational acceleration, and K is the modulus of $\mathbf{K}$.

The long-wave surface orbital velocities computed from the sea surface height data are sampled at the location and time of the active wave breaking fronts. Each location on the sea surface is typically sampled twice by the ATM, while the images are captured continuously. The orbital velocities are computed at the breaking front location at the two available times, and linearly interpolated in time for images captured between the two ATM observations. When the image time falls outside the two surface height measurement times, the orbital velocity is set to the nearest estimate in time. The error in matching the spatial locations of the projected images with the ATM sea surface height data is approximately ±6 m, as estimated from matching the brightest foam patches with enhanced return strength of the ATM.

The intrinsic wave parameters can be estimated from the apparent phase speed and the estimated local orbital velocity. We denote the radian frequency, wavenumber, and phase speed of the intrinsic small wave as σ_i, k_i, and c_i, respectively, and those of the apparent small wave as σ_a, k_a, and c_a, respectively. The relationship between the intrinsic and apparent small wave due to advection by a colinear underlying long-wave orbital velocity can be expressed as (Phillips 1981; Longuet-Higgins 1987; Zhang 2003)

$$\sigma_a = \sigma_i\left[1 + \frac{\sigma_i}{\Sigma}AK\cos\Phi(1 + AK\cos\Phi)\right] \quad \text{and} \tag{15}$$

$$k_a = k_i(1 + AK\cos\Phi), \tag{16}$$

where Σ is the radian frequency of the long wave. Dividing Eq. (15) by Eq. (16), applying the approximation $(1 + AK\cos\Phi)^{-1} = 1 - AK\cos\Phi + O(A^2K^2)$, noting that the apparent speed also includes any surface drift current U_d, and solving for the intrinsic phase speed $c_i = \sigma_i k_i^{-1}$, we obtain

$$c_i = \frac{c_a - AKC\cos\Phi - U_d}{1 - AK\cos\Phi}. \tag{17}$$

When the apparent speed c_a is equal to the long-wave phase speed C, Eq. (17) reduces to $c_i = C - U_d$. Note that Eq. (17) is a 1D equation that applies only when the apparent phase speed c_a is parallel to the long-wave wavenumber K. For 2D velocity vectors, the observed (apparent) breaking velocity is projected to components parallel and perpendicular to the underlying orbital velocity. The parallel component of breaking velocity is adjusted via Eq. (17), and the perpendicular component is adjusted simply by $c_i = c_a - U_d$. The final intrinsic velocity is the vector sum of the two components.

c. Determination of the surface drift current from images

Surprisingly, the advection of the old, inactive foam patches on the sea surface (such as region A in Fig. 4) was not well explained by the orbital velocity obtained from Eq. (14). For example, for this image sequence the mean long-wave orbital velocity along the breaking front was 0.6 m s^{-1}, the mean rear velocity was 3.4 m s^{-1}, and the mean front velocity was 3.9 m s^{-1}. The old foam that remains on the surface from previous wave breaking acts as a passive tracer of the velocity field at the surface. To infer the surface motion, old foam patches are identified based on their area and breaking criteria as in section 5c. For the image sequence evaluated in this paper, the mean old foam velocity is 1.33 ± 0.3 m s^{-1}, 12° to the left of the mean wind direction. This velocity would include effects from the surface current, surface wave orbital velocities, Stokes drift (wave-induced current), and the wind-induced current and is consistent with previously published observations of near-surface currents in the region (Barton et al. 1993; Trasviña et al. 1995).

d. Breaking speed versus underlying phase speed

The use of $\Lambda(c)$ to infer the rate of wave energy dissipation and momentum flux [Eqs. (3) and (5)] depends pivotally on the relationship of the speed of breaking c to the underlying intrinsic phase speed c_i of the breaking wave crest. To our knowledge, no laboratory or field studies have directly examined the advance of the front of the bubble patch with respect to the local underlying phase speed on a wave-by-wave basis. Some insight can be gained from laboratory experiments, however. In studies of unsteady deep-water breaking waves, Rapp and Melville (1990, their section 4.1) measured the intrusion of surface dye to determine the extent and evolution of the mixed (turbulent) region produced by wave breaking. They found that the rear of the mixed region remained essentially stationary while the front initially moved forward at a speed of $c = 0.7$–$0.8c_i$, where c_i was the linear phase speed computed from the center frequency of the wave packet. Note that Banner and Peirson (2007, their appendix B) found that the actual crest speed of steep breaking waves was a factor of 0.9 ± 0.04 less than the linear phase speed. Stansell and

MacFarlane (2002) performed a comprehensive laboratory analysis of the ratio of particle velocity at the crest of a breaking wave to the wave crest (phase) speed. They found that this ratio is at most 0.95 for spilling breakers and 0.81 for plunging breakers.

Assuming that the motion of the bubble patch during active breaking follows the fluid particle velocity or the turbulent patch produced by breaking, the laboratory data indicate a linear relationship,

$$c = \kappa c_i, \tag{18}$$

where κ is in the range of 0.7–0.95.

Although laboratory experiments show a linear relationship between the underlying phase speed and the speed of breaking, field observations of wave-breaking speeds include effects that are often not present in the laboratory, such as advection from the orbital velocity of longer waves and the surface drift current.

A comparison of the $\Lambda(c)$ distributions is presented in Fig. 11 after corrections for the three issues raised above: adjustment from breaking speed to underlying phase speed by the factor κ [Eq. (18)], correction for underlying long-wave orbital velocity [Eq. (17)], and correction for surface drift current U_d. Although the distributions are tightly clustered, it is seen that correcting for the orbital velocity (solid lines) results in a minor adjustment to the $\Lambda(c)$ distributions, especially considering the range of $\Lambda(c)$ distributions as the thresholds are varied (Fig. 5). Correcting for both orbital and surface current velocities (dashed lines) shifts the peak of $\Lambda(c)$ to lower speeds and decreases the power-law slope of $\Lambda(c)$ in the range $4 < c < 10$ m s^{-1}. This is essentially because subtraction of a constant speed is a greater fraction of the low speeds than the fast speeds. The red curves show the result when the breaking velocity is *first* adjusted by the factor $\kappa = 0.9$ in Eq. (18) and *then* corrected for orbital velocity (solid line) as well as surface current (dashed line) according to Eq. (17). Adjustment of the breaking speed to the local phase speed by κ shifts the $\Lambda(c)$ distributions toward faster speeds. The integral under all $\Lambda(c)$ distributions is equal, except for the dashed black line, where the raw breaking speed has been corrected for orbital velocity and surface current. The area under this distribution decreased by 8% because some of the slow-breaking waves resulted in negative velocities after the transformations.

e. Effect of resolution in space and time

For the image sequence under consideration the projected images had a pixel width of 0.30 m and an image sampling rate of $\Delta t = 0.1333$ s. This results in a minimum discrete resolvable speed of 1 pixel between successive images, or $c_d = \Delta x/\Delta t = 2.25$ m s^{-1}.[5] To ascertain the effect of resolution on the $\Lambda(c)$ distribution, images were subsampled in both space and time, resulting in different minimum resolvable speeds c_d. Although the peak of $\Lambda(c)$ decreased with decreasing c_d, it could not alone explain the peak and the reduced value of $\Lambda(c)$ at low speeds.

Gemmrich et al. (2008) notably found a peak in the $\Lambda(c)$ distribution, although they had very high image resolution. This also indicates that the decreased values of $\Lambda(c)$ at low wave speeds, in contrast to Phillips's theory, may not be due to image-resolution effects. The large amounts of low-speed breaking found in the laboratory by Jessup and Phadnis (2005) using infrared imaging of microscale breaking indicate that some of the wave energy dissipation predicted by Phillips's theory at low breaking speeds is due to breakers that do not entrain an optically thick bubble cloud. Furthermore, differences between the intrinsic wave phase speed and the observed breaking speed are enhanced at the low speeds. Further field experiments with high spatial resolution as well as infrared observations are needed to observe the $\Lambda(c)$ distributions for low speeds.

f. Aircraft motion removal

As mentioned in section 5, it was found from calibration flights over the airport ramp that the earth-referenced images had a mean error (or drift) of less than 0.13 m s^{-1}, with a standard deviation of 1 m s^{-1} when the images are subsampled at 7.5 Hz, as was done in this analysis (see Kleiss 2009). The low mean error of 0.13 m s^{-1} can be attributed to correct determination of camera position and orientation at the time of image capture and to proper correction of lens distortion. The standard deviation of 1 m s^{-1} results from the separation of the IMU from the camera and reflects the vibrations and flexing of the aircraft. The calibration images were captured at a typical altitude of 500 m. To insure proper removal of aircraft motion from images captured over the ocean surface, only field images captured at typical altitudes of 350–400 m (close to 500 m) were considered for the $\Lambda(\mathbf{c})$ processing.

Extreme care was taken to validate that the aircraft motion was removed. Most field image sequences were taken in the downwind or upwind directions, and a few image sequences were taken in the crosswind direction. The final results—including $\Lambda(\mathbf{c})$, whitecap coverage, breaking rate, and image-to-ATM matching—did not show any consistent bias or trends associated with the flight direction or altitude. For this reason, we feel

[5] Note that the $\Lambda(c)$ distributions show speeds with $c < c_d$ because the whitecap contours and the ellipse centroids were determined to subpixel accuracies.

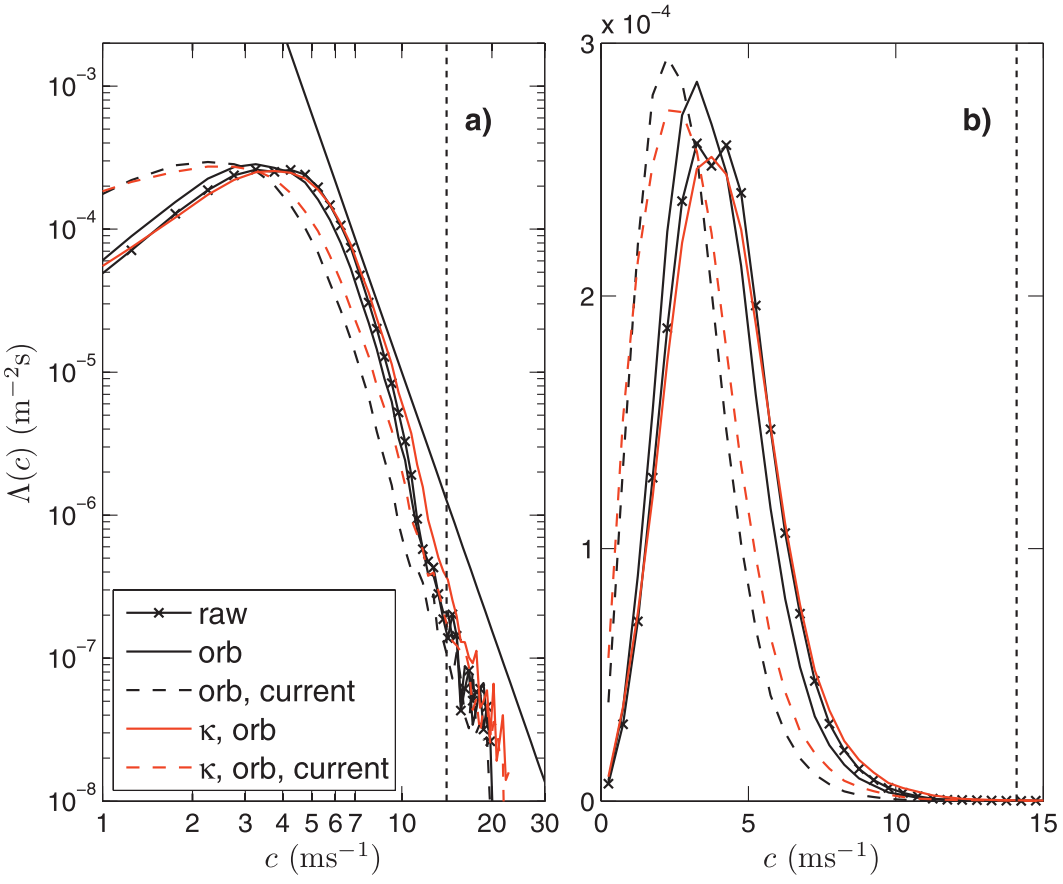

FIG. 11. The $\Lambda(c)$ distribution from the contour method, using the elemental, translational speeds, and the effect of correcting for the difference between breaking speed and phase speed (κ), surface current, and orbital velocity. The $\Lambda(c)$ distributions are from the observed breaking speeds (line with times signs); velocity corrected for long-wave orbital velocities (solid black line); correction of both long-wave orbital velocities and surface drift current (black dashed line); correction of phase speed by the factor $\kappa = 0.9$ and long-wave orbital velocities (red solid line); and correction of phase speed, long-wave orbital velocities, and surface current (red dashed line). The vertical dotted black line indicates the spectral peak phase speed of 14.1 m s^{-1}. Shown are (a) logarithmic coordinates and (b) linear coordinates, and the diagonal black line in (a) represents the function $10c^{-6}$.

confident that the estimate of aircraft motion errors over the airport ramp is applicable to the field images.

g. *Comparison with previous studies*

The results of this study are compared with the results of Melville and Matusov (2002) and Gemmrich et al. (2008), using methods as close as possible to those published. For comparison with the Melville and Matusov results, elemental speeds are computed using bulk- and finescale PIV-type correlation rather than bulk-scale correlation and optical flow, and the mean rear velocity is removed from each breaking observation. The mean rear velocity, as a function of time, of each whitecap observation is identified using the inverse of the seven criteria listed in section 5c. The elemental breaking speed with the mean rear velocity vector subtracted is denoted c_{rr}. It is verified that c_{rr} is still directed outward from the contour. Figure 12a shows the resulting $\Lambda(c_{\mathrm{rr}})$ distribution (black line with times signs) in comparison with the empirical form of $\Lambda(c)$ presented in Melville and Matusov (2002) as a black solid line:

$$\Lambda(c)(10/U_{10})^3 = 3.3 \times 10^{-4} \exp(-0.64c). \qquad (19)$$

The GOTEX $\Lambda(c_{\mathrm{rr}})$ distribution is described by the exponential form $\Lambda(c)(10/U_{10})^3 = 4.4 \times 10^{-4} \exp(-0.82c)$. This line is plotted in Fig. 12a but describes the data so well that it is barely visible. The different exponent may be due to the less-developed, stronger-forced, and colinear wind and wave conditions in the Gulf of Tehuantepec relative to the Shoaling Waves Experiment (SHOWEX) dataset used in Melville and Matusov (2002). For example, the Tehuantepec breaking crests

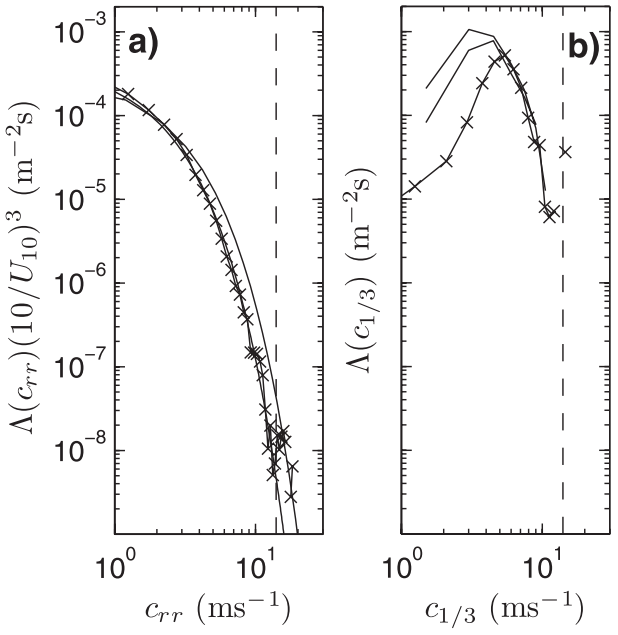

FIG. 12. The $\Lambda(c)$ distributions from the GOTEX data processed consistently with methods used by (a) Melville and Matusov (2002) and (b) Gemmrich et al. (2008). In (a), the line with times signs is the GOTEX dataset processed using the contour method with PIV-only elemental speeds and the mean rear velocity removed (c_{rr}), and the solid line is the empirical fit from Melville and Matusov (2002) [Eq. (19)]. In (b), the line with times signs is the GOTEX dataset processed with the ellipse method, using the top 1/3 speed and the maximum length for each breaking event, and the solid lines are the $\Lambda(c)$ result from Gemmrich et al. (2008) for the fully developed sea state (their wave age $c_p/u_* = 33$). The vertical dashed line shows the spectral peak phase speed for this GOTEX image sequence.

generally appear to be more crescent shaped, as in region C in Fig. 4, than the SHOWEX data. The difference may also be affected by the along-crest-length smoothing employed in Melville and Matusov (2002) that was not implemented here. The fundamental difference between the present contour method with elemental speeds (Fig. 5) and the result shown in Fig. 12a involves the removal of the rear velocity of the foam patch. In an otherwise stationary earth reference frame, the velocity at the rear of the bubble patch is due to degassing of the foam patch, advection of the bubbles with the fluid flow upon initiation of breaking, and straining by the underlying orbital velocity. Removal of the rear velocity was motivated by the laboratory experiments of Rapp and Melville (1990), which found that the rear of the turbulent patch, visualized with a dye tracer, remained stationary to leading order. It appears that this assumption breaks down in the field, however, possibly because of the different spatial extent of the turbulence patch in comparison with the optically thick bubble patch over the duration of active breaking. Furthermore, the nonstationary sea surface, caused by surface currents and any residual camera motion, would affect the earth-referenced $\Lambda(c)$ estimates in Fig. 5 but not Fig. 12a.

The method of Thomson and Jessup (2009) was not directly employed in this study. They presented a comparison of their Fourier-based method with time-domain methods akin to the temporal method [$c(t)$] and event method c_i discussed above. Their Fourier-based method is shown to agree best with their time-domain average instantaneous (temporal) method, except for low speeds ($c < 1$ m s^{-1}) at which the temporal method is positively biased because of their event-based correction for the advection by long waves. In practice, the Fourier-based method should fall somewhere between the temporal and elemental interpretations of breaking speed, because the transformation from the frequency f and wavenumber k of the thresholded images to a binned length of breaking with a speed $c = f/k$ results in some spectral spreading of the individual, temporal translations (J. Thomson 2010, personal communication).

In Fig. 12b, the GOTEX data are processed in a manner similar to Gemmrich et al. (2008), as described in section 6. The black solid lines show the $\Lambda(c)$ results from Gemmrich et al. (2008) for the fully developed cases (their cases II and III), with wave age $c_p/u_* = 33$ and 10-m wind speed of 11.5 and 12.5 m s^{-1}. Thus the sea state and wind speed in Gemmrich et al. (2008) are close to the conditions of the present study (Table 1). Gemmrich et al. (2008) obtain the scale of breaking from each breaking event by considering the mean of the top one-third highest speeds for each tracked breaking event. This approach, which was not explained in their paper, may be an attempt to tie the speed of breaking more closely to the phase speed of the breaking wave. They also only consider the maximum length of the breaker during an event.

When the ellipse method is employed in a fashion similar to Gemmrich et al. (2008), the $\Lambda(c)$ distributions show nearly perfect agreement for $c_{1/3} > 5$ m s^{-1}, down to the high-speed end of the distribution (black line with times signs). The implementation of the ellipse method on the GOTEX data reaches a peak at $c = 5$ m s^{-1}, whereas the Gemmrich et al. (2008) data obtain peak values at $c = 2$–3 m s^{-1}. This may be due to the much higher resolution of the Gemmrich et al. (2008) data (2- vs 30-cm resolution).

The speed, length, and area of breaking evolve in time, as shown in Fig. 13. To observe the breaking waves for a longer time, an image sequence was captured as the aircraft ascended from 450 to 1160 m, corresponding to image residence times of 3–7 s. This image sequence

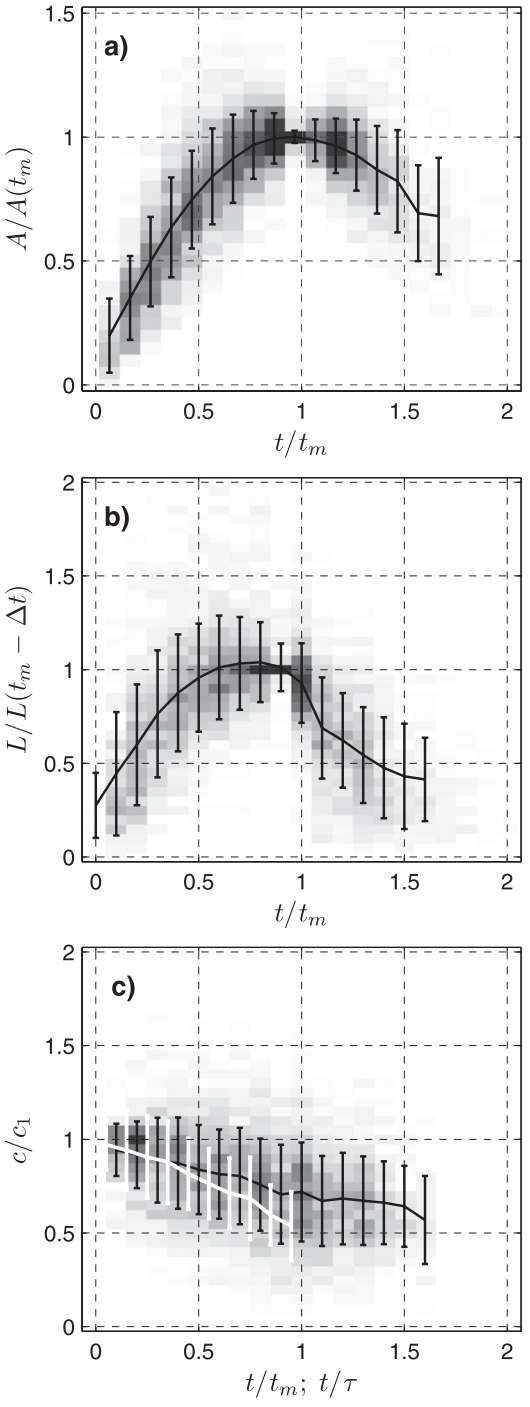

FIG. 13. The evolution of the area A, length L, and speed c of breakers with time t for whitecaps that begin breaking in our field of view. Time is normalized by t_m, the time at which each whitecap obtains its maximum area as determined by a parabolic fit to the whitecap area as a function of time. (a) Foam patch area normalized by the area at time t_m. (b) Length of breaking normalized by the breaking length the observation before the whitecap reaches maximum area. (c) Speed of breaking normalized by the initial speed c_1. The black line in (a)–(c) shows the bin average, with error bars corresponding to 1 std dev. The white line in (c) shows laboratory results, where time is normalized by the breaking duration τ, and white error bars correspond to 1 std dev.

was captured on the afternoon of research flight 5, on 17 February 2004, at a fetch of 225 km, with 10-m wind speed of 17.0 m s^{-1}, effective friction velocity of 0.65 m s^{-1}, and dominant phase speed of 12.8 m s^{-1}. Time is normalized by t_m, the time at which whitecaps obtain their maximum area as determined by a parabolic fit to the whitecap area as a function of time (Fig. 1a). The value of t_m ranges from 0.27 to 4.4 s for this image sequence. Only breaking events that begin while in the field of view, obtain a peak in the foam area, and actively break for least $t_\tau = 0.67$ s are considered. This constitutes 21% of the active breakers in this image sequence.

On average, we see that the length of breaking increases to roughly the maximum length of breaking at one-half the time it takes for the whitecap to obtain its maximum area. The breaker maintains this length until the whitecap obtains its maximum area, at which time the length of breaking decreases. The length of breaking is normalized by the length of breaking that is observed the image *before* the whitecap reaches maximum area. This is because the change in whitecap area is one of the criteria for active breaking, and we wished to avoid a sudden change in these criteria when normalizing. Note that active breaking is still observed while the foam patch area is decreasing, despite the foam patch area criterion.

The mean speed of breaking decreases to a factor of about 0.7 of the initial breaking speed c_1 when the whitecap obtains maximum area, and it continues to decrease to a factor of about 0.55 of the initial speed as the foam patch area decreases and breaking subsides. This result was validated with laboratory experiments in a glass channel with a wave maker generating a focusing wave packet (P. Sutherland 2009, personal communication; cf. Rapp and Melville 1990; Drazen et al. 2008) in freshwater of 60-cm depth. The laboratory data are normalized temporally by the duration of breaking τ rather than t_m because of difficulties measuring foam patch area in the laboratory setup. The mean breaking speed in the laboratory, averaged over 16 runs with a range of wave frequencies and slopes, decreased to a factor of 0.5 times the initial speed of breaking, roughly consistent with the decreasing speed of breaking observed in the field, over the entire duration of breaking.

In Phillips's (1985) formulation, $\Lambda(c)\,dc$ is the *mean* total length of breaking crests per unit sea surface area with speed c. Taking the mean of the top 1/3 speeds and the maximum length of each breaking event as in Gemmrich et al. (2008) does not result in a distribution of the mean total length of breaking crests. In both the laboratory and the field, both the breaking length and speed exhibited a large amount of variability for each breaking event, such that taking the maximum length or

the top 1/3 of the speeds would often be affected by the largest instantaneous measurements.

From Fig. 13, we parameterize the speed of breaking as a simple function, $c(\hat{t}) = c_1(1 - 0.4\hat{t})$, where $\hat{t} = t/t_m$, and the length of breaking as $L(\hat{t}) = L_{\max}(a_1\hat{t}^2 + a_2\hat{t} + a_3)$, with $a_1 = -1.6$, $a_2 = 2.24$, and $a_3 = 0.24$. The contribution of a single breaking event to the first moment of $\Lambda(c)$ can be thought of as the cumulative area swept by the breaker

$$\int c(\hat{t})L(\hat{t})\,d\hat{t} = \int_0^{1.5} c_1 L_{\max}(1 - 0.4\hat{t})(a\hat{t}^2 + b\hat{t} + c)\,d\hat{t}. \quad (20)$$

If one integrates over $0 < \hat{t} < 1.5$, the mean contribution to the first moment is $0.8c_1L_{\max}$. If one takes the mean of the top 1/3 speeds and the maximum breaking length, however, the contribution to the first moment is $1.4c_1L_{\max}$, which is 75% higher than the mean contribution. Likewise, the contribution of a single breaking event to the fifth moment of $\Lambda(c)$, which is related to the wave dissipation, can be expressed as

$$\int c(\hat{t})^5 L(\hat{t})\,d\hat{t} = \int_0^{1.5} c_1^5 L_{\max}(1 - 0.4\hat{t})^5(a\hat{t}^2 + b\hat{t} + c)\,d\hat{t}. \quad (21)$$

If one integrates over $0 < \hat{t} < 1.5$, the mean contribution to the fifth moment is $0.3c_1^5L_{\max}$ while the top 1/3 speed and the maximum length contribute $0.9c_1^5L_{\max}$, which is 3 times the mean contribution. Using the maximum length of breaking and the mean of the fastest 1/3 breaking speeds results in a $\Lambda(c)$ distribution that does not reflect the definition as given in Phillips (1985) and also results in moments of $\Lambda(c)$ that are positively biased.

9. Conclusions

This paper discusses methods of video image processing to determine the length and speed of breaking crests. Distribution $\Lambda(c)\,dc$, which is the average total length of breaking waves per unit sea surface area with breaking speed between c and $c + dc$, offers a scale-dependent description of wave breaking that is valuable for understanding air–sea fluxes of gas and primary marine aerosols, wave energy dissipation, and momentum flux from the wave field to the surface current. In particular, we discuss the determination of wave breaking kinematics from video images and the effect on the resulting $\Lambda(c)$ distribution.

Wave breaking often creates complicated structures of bubbles and foam on the sea surface. The speed of breaking varies both along the breaking crest and with time. Although one may attribute a single speed of breaking to a breaking event, or at each observed time of breaking, the most complete description of breaking speed is determined as a function of both space and time; what is called the *elemental* method in this paper. The breaking speed can be considered as either the full translational speed of breaking, or the component that is normal to the breaking wave crest. Figures 6 and 10 compare the $\Lambda(c)$ distributions for different definitions of breaking velocity. The elemental velocity contains the most information, as the temporal and event-average velocity can be computed from it.

The determination of actively breaking fronts is not trivial in video images of the sea surface. Two methods of identifying actively breaking wave crests are presented: the contour method and the ellipse method. The contour method identifies foam patches by a brightness threshold on the image and then determines the portions of the foam patch perimeters that are actively breaking. This method produces a complete description of the kinematics around the entire foam patch perimeter, as well as corresponding information on the foam patch area and morphology. The ellipse method determines breaking fronts using a threshold on the difference of two consecutive images, providing information on the actively breaking crest alone. The sensitivity of the $\Lambda(c)$ distributions to the thresholds used in the analysis is shown in Figs. 5 and 8. Both methods appear to be sensitive to the thresholds for the slower breaking speeds, and are less sensitive in the region of the high-speed tail. The general shape of the $\Lambda(c)$ distribution is consistent for the two methods, but the ellipse method generally gives a longer breaking crest length, is tracked for a longer time for fast ($c > 4$ m s^{-1}) breaking, and yields fewer observations of slow breaking.

Notably, the $\Lambda(c)$ distributions published by Melville and Matusov (2002) and Gemmrich et al. (2008) are qualitatively obtained with the present dataset when the processing method and the definition of breaking speed are implemented as in those studies. This highlights the importance of careful consideration of the processing method, choice of threshold, and definition of breaking speed when calculating $\Lambda(c)$ from sea surface imagery. In particular, it appears that the rear of the foam patch shows a translation greater than the background orbital velocity—it may be affected by degassing of the large, optically thick bubbles and advection by the breaking crest at the initiation of breaking. Furthermore, defining the breaking speed as the mean of the top 1/3 speeds, and the length of breaking as the maximum breaking length is not consistent with Phillips's definition of $\Lambda(c)$ as the total mean length of breaking with speed c per unit sea

surface area, per speed increment. Such definitions positively bias the first and fifth moments of $\Lambda(c)$ by 75% and 300%, respectively.

Previous studies of $\Lambda(c)$ have considered the relationship of the breaking rate to the first moment of $\Lambda(c)$ [Eq. (1)] as a validation tool for the $\Lambda(c)$ distributions (Jessup and Phadnis 2005; Gemmrich et al. 2008; Thomson and Jessup 2009). Both the breaking rate R and the total observed length of breaking are sensitive to the choice of thresholds, and the definition of breaking, such that the comparison in Eq. (1) is generally of more utility as a consistency check on the processing than as a physical validation of the observations.

The observed speed of breaking on the sea surface may be affected by the orbital velocity of underlying longer waves and the surface drift current. Furthermore, laboratory studies have indicated that the maximum particle speed of the breaking crest is slightly less than the phase speed of the wave that is breaking. The peak of the $\Lambda(c)$ distributions shifts toward slower speeds after correction of the estimated surface current. The effect of straining by the underlying orbital velocity and the difference between breaking and phase speed does not affect the $\Lambda(c)$ distributions beyond the limits from the range of thresholds. However, these corrections will bear more impact on application of $\Lambda(c)$, such as the wave energy dissipation that scales like the fifth moment of $\Lambda(c)$ [Eq. (3)].

Acknowledgments. We thank Peter Sutherland for providing laboratory data describing the evolution of the speed of breaking with time. We acknowledge the collaboration of Carl A. Friehe (co–chief scientist for the GOTEX project) and Djamal Khelif at the University of California, Irvine. We are grateful to Allen Schanot, Henry Boynton, Lowell Genzlinger, Ed Ringleman, and support staff at NCAR Research Aviation Facility for making the flight operations and related logistics possible. We thank Bill Krabill, Bob Swift, Jim Yungel, John Sonntag, and Robbie Russell at NASA/EG&G, for the deployment and data postprocessing of the ATM. We are grateful to Leonel Romero for providing the wind and wave data. We thank Peter Matusov for helpful comments and discussions in the initial stages of this work. We acknowledge the engineering and logistical support from Jim Lasswell and from Axel Pierson at Scripps Institution of Oceanography. This research was supported by grants from the National Science Foundation (Ocean Sciences) and ONR (Physical Oceanography) to WKM. JK was also supported by an NSF Graduate Student Fellowship and a National Defense Science and Engineering Graduate Student Fellowship.

REFERENCES

Banner, M. L., and W. L. Peirson, 2007: Wave breaking onset and strength for two-dimensional deep-water wave groups. *J. Fluid Mech.,* **585,** 93–115, doi:10.1017/S0022112007006568.

Barton, E. D., and Coauthors, 1993: Supersquirt: Dynamics of the Gulf of Tehuantepec, Mexico. *Oceanography,* **6,** 23–30.

Bondur, V. G., and E. A. Sharkov, 1982: Statistical properties of whitecaps on a rough sea. *Oceanology,* **22,** 274–279.

Bouguet, J.-Y., cited 2006: Camera calibration toolbox for Matlab. [Available online at http://www.vision.caltech.edu/bouguetj/calib_doc/.]

Brown, E. N., C. A. Friehe, and D. H. Lenschow, 1983: The use of pressure fluctuations on the nose of an aircraft for measuring air motion. *J. Climate Appl. Meteor.,* **22,** 171–180.

Callaghan, A. H., and M. White, 2009: Automated processing of sea surface images for the determination of whitecap coverage. *J. Atmos. Oceanic Technol.,* **26,** 383–394.

Drazen, D. A., W. K. Melville, and L. Lenain, 2008: Inertial scaling of dissipation in unsteady breaking waves. *J. Fluid Mech.,* **611,** 307–332.

Duncan, J. H., 1981: An experimental investigation of breaking waves produced by a towed hydrofoil. *Proc. Roy. Soc. London,* **A377,** 331–348.

Fleet, D. J., 1992: *Measurement of Image Velocity*. Kluwer Academic, 224 pp.

Gemmrich, J. R., M. L. Banner, and C. Garrett, 2008: Spectrally resolved energy dissipation rate and momentum flux of breaking waves. *J. Phys. Oceanogr.,* **38,** 1296–1312.

Holland, K. T., R. A. Holman, T. C. Lippmann, J. Stanley, and N. Plant, 1997: Practical use of video imagery in nearshore oceanographic field studies. *IEEE J. Oceanic Eng.,* **22,** 81–92.

Hornberg, A., 2007: *Handbook of Machine Vision*. Wiley-VCH, 822 pp.

Jessup, A. T., and K. R. Phadnis, 2005: Measurement of the geometric and kinematic properties of microscale breaking waves from infrared imagery using a PIV algorithm. *Meas. Sci. Technol.,* **16,** 1961–1969.

Jones, I. S. F., and Y. Toba, 2001: *Wind Stress over the Ocean.* Cambridge University Press, 326 pp.

Kleiss, J. M., 2009: Airborne observations of the kinematics and statistics of breaking waves. Ph.D. dissertation, Scripps Institution of Oceanography–University of California, San Diego, 218 pp.

——, and W. K. Melville, 2010: Observations of wave-breaking kinematics in fetch-limited seas. *J. Phys. Oceanogr.,* **40,** 2575–2604.

Krabill, W. B., and C. F. Martin, 1987: Aircraft positioning using global positioning system carrier phase data. *Navigation,* **34,** 1–21.

Lighthill, J., 1978: *Waves in Fluids*. Cambridge University Press, 504 pp.

Longuet-Higgins, M. S., 1969: A nonlinear mechanism for the generation of sea waves. *Proc. Roy. Soc. London,* **A311,** 371–389.

——, 1987: The propagation of short surface waves on longer gravity waves. *J. Fluid Mech.,* **177,** 293–306.

Ma, Y., S. Soatto, J. Kŏsecká, and S. S. Sastry, 2004: *An Invitation to 3-D Vision.* Springer, 526 pp.

Melville, W. K., 1994: Energy dissipation by breaking waves. *J. Phys. Oceanogr.,* **24,** 2041–2049.

——, 1996: The role of surface-wave breaking in air–sea interaction. *Annu. Rev. Fluid Mech.,* **28,** 279–321.

——, and P. Matusov, 2002: Distribution of breaking waves at the ocean surface. *Nature,* **417,** 58–63.

Mironov, A. S., and V. A. Dulov, 2008: Detection of wave breaking using sea surface video records. *Meas. Sci. Technol.,* **19,** 015405, doi:10.1088/0957-0233/19/1/015405.

Monahan, E. C., 1993: Occurrence and evolution of acoustically relevant sub-surface bubble plumes and their associated, remotely monitorable, surface whitecaps. *Natural Physical Sources of Underwater Sound,* B. R. Kerman, Ed., Springer, 503–517.

Phillips, O. M., 1981: The dispersion of short wavelets in the presence of a dominant long wave. *J. Fluid Mech.,* **107,** 465–485.

——, 1985: Spectral and statistical properties of the equilibrium range in wind-generated gravity waves. *J. Fluid Mech.,* **156,** 505–531.

——, F. L. Posner, and J. P. Hansen, 2001: High range resolution radar measurements of the speed distribution of breaking events in wind-generated ocean waves: Surface impulse and wave energy dissipation rates. *J. Phys. Oceanogr.,* **31,** 450–460.

Raffel, M., C. Willert, S. Wereley, and J. Kompenhans, 2007: *Particle Image Velocimetry: A Practical Guide*. 2nd ed. Springer, 448 pp.

Rapp, R. J., and W. K. Melville, 1990: Laboratory measurements of deep-water breaking waves. *Philos. Trans. Roy. Soc. London,* **A331,** 735–780.

Romero, L., and W. K. Melville, 2010: Airborne observations of fetch-limited waves in the Gulf of Tehuantepec. *J. Phys. Oceanogr.,* **40,** 441–465.

Stansell, P., and C. MacFarlane, 2002: Experimental investigation of wave breaking criteria based on wave phase speeds. *J. Phys. Oceanogr.,* **32,** 1269–1283.

Steenburgh, W. J., D. M. Schultz, and B. A. Colle, 1998: The structure and evolution of gap outflow over the Gulf of Tehuantepec, Mexico. *Mon. Wea. Rev.,* **126,** 2673–2691.

Sugihara, Y., H. Tsumori, T. Ohga, H. Yoshioka, and S. Serizawa, 2007: Variation of whitecap coverage with wave-field conditions. *J. Mar. Syst.,* **66,** 47–60.

Thomson, J., and A. T. Jessup, 2009: A Fourier-based method for the distribution of breaking crests from video observations. *J. Atmos. Oceanic Technol.,* **26,** 1663–1671.

——, J. R. Gemmrich, and A. T. Jessup, 2009: Energy dissipation and the spectral distribution of whitecaps. *Geophys. Res. Lett.,* **36,** L11601, doi:10.1029/2009GL038201.

Thorpe, S. A., and A. J. Hall, 1983: The characteristics of breaking waves, bubble clouds, and near-surface currents observed using side-scan sonar. *Cont. Shelf Res.,* **1,** 353–384.

Trasviña, A., E. D. Barton, J. Brown, H. S. Velez, P. M. Kosro, and R. L. Smith, 1995: Offshore wind forcing in the Gulf of Tehuantepec, Mexico: The asymmetric circulation. *J. Geophys. Res.,* **100** (C10), 20 649–20 663.

Zhang, X., 2003: Observation on modulation of short wind waves. *Proc. IEEE Int. Geoscience and Remote Sensing Symp.,* Vol. 4, IEEE, 2697–2699.